FLASH X-RAY TOMOGRAPHY OF KOLSKY BAR EXPERIMENTS

by

Hangjie Liao

A Dissertation

Submitted to the Faculty of Purdue University

In Partial Fulfillment of the Requirements for the degree of

Doctor of Philosophy

School of Aeronautics & Astronautics

West Lafayette, Indiana

May 2018

THE PURDUE UNIVERSITY GRADUATE SCHOOL
STATEMENT OF COMMITTEE APPROVAL

Dr. Weinong Chen, Chair
School of Aeronautics and Astronautics
Dr. Charles Bouman
School of Electrical and Computer Engineering
Dr. James Doyle
School of Aeronautics and Astronautics
Dr. Michael Sangid
School of Aeronautics and Astronautics
Dr. Tyler Tallman
School of Aeronautics and Astronautics

Approved by:
Dr. Weinong Chen
Head of the Graduate Program

TABLE OF CONTENTS

LIST OF TABLES

LIST OF FIGURES

ABSTRACT

Author: Liao, Hangjie. PhD
Institution: Purdue University
Degree Received: May 2018
Title: Flash X-ray Tomography of Kolsky Bar Experiments.
Major Professor: Weinong Chen

Kolsky bar is commonly used to characterize materials at high strain rates from 10^2 to 10^4/s. In-situ visualization of specimen fracture process is vital to understand its dynamic mechanical behaviors. In this dissertation, compression Kolsky bar is combined with a high speed multichannel flash X-ray tomography methodology to capture snapshots of the dynamic in-situ 3D specimen volume information to visualize the dynamic damage and fracture process. This method is capable to produce sub-millimeter-resolution tomography reconstructions of dynamic fracture process from very limited number (4 in this research) of projections. This method enables a precise and repeatable control over the loading history of the specimen and the flash X-ray projection time, thus a correlation between the stress-strain/force-displacement response and the reconstructed volume can be clearly defined. The 4-channel flash X-ray setup is built for low geometric unsharpness (0.15 mm) to improve reconstruction resolution by placing intraoral size phosphor storage plate detectors close to the specimen without interference from unnecessary exposures.

For each 2D projection, raw image scanned from detector was aligned according to the positions of the Kolsky bars in the projection via edge detection. Dark current was measured for each experiment and imposed to the reconstruction log input. The log inputs with and without the normalization to the un-deformed state were used. To reduce number of artifacts, Algebraic Reconstruction Technique was used to iteratively update the reconstruction. Three different static phantoms were imaged and reconstructed, where the result shows the image processing inputs are correct and the relative locations of X-ray beams, specimen and phosphor storage plate (PSP) detectors are within the tolerance. Three sets of preliminary Kolsky bar experiments were conducted, where the results indicate that a good tomography reconstruction requires a sufficient feature-signal-to-noise ratio in the 2D projection and a small number of cracks inside the specimen for reduced number of artifacts.

Applying this technique, dynamic spheroconical indentation experiments on two types of machinable ceramics (Macor and Mykroy/Mycalex 550) and uniaxial compression on 3D printed sandstone around 100/s were conducted. For indentation experiments, the post-peak-force reconstructions show that the Macor specimen fractures due to two major cracks - one parallel and the other one oblique to the loading direction, while the M/M specimen breaks due to only one major crack parallel to the loading. Such finding matches with the cross-sectional microstructure images, where the particle is randomized distributed in Macor, while the particle is highly directional in M/M. For 3D printed sandstone, it is found that the adhesive infiltrant coated layer apparently affects its mechanical behaviors: the specimen with higher percentage of coated region has higher strength. Under ~100/s loading, the 3D printed sandstone exhibits a brittle behavior, and the reconstructions show that the cylindrical specimen fractures due to cracks separating the side coated layer. Such cracks are initialed near one of specimen-bar interfaces. Under 0.001/s loading, however, the sandstone exhibits a ductile behavior, and the crack is initialed from the center of the specimen. Based on the reconstruction results, the limitations and several potential improvements of the flash X-ray tomography are discussed.

CHAPTER 1. INTRODUCTION

1.1 Background

Understanding material behaviors at elevated strain rates is essential when designing and analyzing structures in dynamic or impact applications. Many materials have been found to be rate-sensitive [2,3], where the quasi-static analysis alone is insufficient to represent their mechanical response. For example, Poly(methyl methacrylate) or PMMA has been reported its Young's Modulus increases from 1.7 GPa subjected to 0.001/s quasi-static loading to 123 GPa subjected to 4300/s dynamic loading, and it behaves elastic-plastically under quasi-static compression while it fractures in a brittle way under dynamic compression [18]. To ensure structural integrity and instrument function properly at dynamic strain rate conditions, accurate material constitutive models along with material failure behaviors need to be obtained. These material constitutive models can be obtained via recording average stress-strain information of the specimen at given loading conditions. And the failure behaviors can be obtained by observing the weak points and the type of failure (such as tensile failure and shear failure) during the deformation. To accomplish these two, researchers could combine 1) a robust and repeatable loading device which is capable to load the specimen at desired dynamic strain rates and records average stress-strain response, and 2) an in-situ imaging system which has fast enough response time and is able to synchronize with the loading device.

Chiefly among many experimental techniques, loading frame (e.g. MTS), drop tower, and Kolsky bar experiments are most common adopted loading devices to test materials depending on the application. The loading frame, which is powered by hydraulic or electro-mechanical actuators to load the specimen, is generally used to test within the quasi-static strain rate range (which is usually defined as 10^{-4}/s to 10^{0}/s). The main advantage of loading frame is that the movement of the actuator can be accurately controlled within certain limits (response time, maximum acceleration and maximum power). When the desired testing strain rate is in the range of intermediate strain rates (which is usually defined as 10^{0}/s to 10^{2}/s), drop tower is commonly used to supply the loading speed by a free-fall dropping weight impacting the test subject. It is noted that the specimen strain rate during the impact event of drop tower experiment is decreasing with respect to time, since the kinetic energy of the drop weight gradually transfers to the strain energy of the specimen.

In most cases, for the easiness to interpret a set of stress-strain data to a rate-dependent constitutive model, it is desired for the specimen been deformed under constant strain rate. To compensate this drawback of drop tower, high speed MTS operated in open-loop mode [2] and long Kolsky bar (or LSHPB) [19] are used. For experiments in the dynamic strain rate region of 10^2/s to 10^4/s, conventional Kolsky bars (or split Hopkinson bars) are usually used [1,2].

1.2 Kolsky Bar Techniques

Since originally developed by Kolsky [1] in 1949, the Kolsky bar has been modified and improved by many researchers [2, 3]. Frew [4] attached a copper pulse shaper on front of incident bar to shape the stress pulse and reduce the high frequency oscillations. Song [2] used a flange attached on incident bar to stop the movement of the bar system after a pre-defined travel distance to prevent multiple loadings on the specimen. The Kolsky bar was also extended its application to tension [5], torsion [6], and tri-axial compression [7] loading conditions. With those modifications and extensions for the Kolsky bar, the dynamic stress-strain response of the material averaged over the entire specimen volume can be effectively obtained in a repeatable way.

While there is still no published standard for the Kolsky bar yet, a common design for compressive Kolsky bar is shown in Figure 1.1.

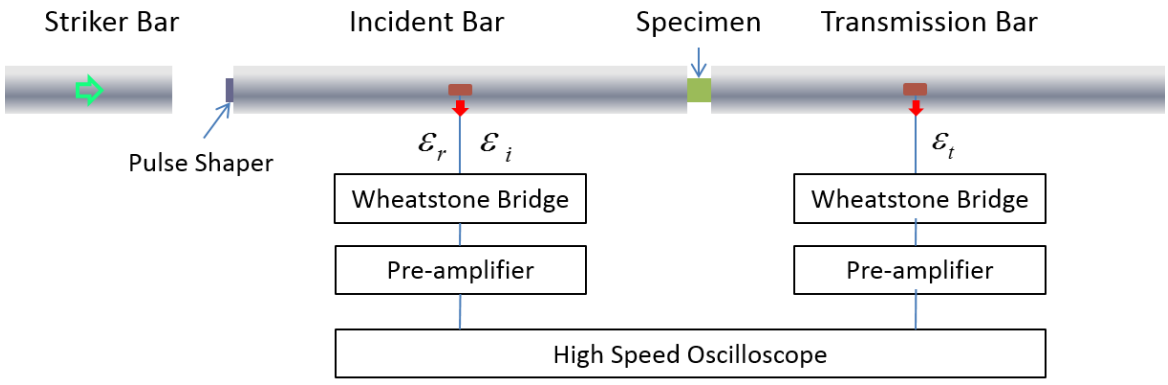

Figure 1.1 Schematic of compressive Kolsky bar.

As shown in Figure 1.1, a sample is sandwiched by two elastic long bars (incident and transmission bars). A striker bar is lunched to impact the incident bar to generate a stress wave (called incident wave), where the pulse shaper is used to eliminate the high frequency oscillations due to metal-

metal impact and shape the incident wave to a desired shape. This incident wave propagates through the incident bar to specimen interface and deforms the specimen. At the same time part of the energy transmits to transmission bar and forms transmission wave ε_t, and another part of the energy reflects back to incident bar and forms reflected wave ε_r. These three waves can be recorded by strain gages on both bars and digitized by a high-speed oscilloscope. With 1-D wave propagation theory and assumption of stress equilibrium between two specimen-bar ends [2], the averaged specimen strain rate history and stress-strain response can be obtained by Equation 1.1-1.3:

$$\dot{\varepsilon}(t) = 2\frac{c_b \varepsilon_r(t)}{l_s} \tag{1.1}$$

$$\varepsilon(t) = 2\int_0^t \frac{c_b \varepsilon_r(\tau)}{l_s} d\tau \tag{1.2}$$

$$\sigma(t) = \frac{E_b A_b \varepsilon_t(t)}{A_s} \tag{1.3}$$

where c_b is the bar wave speed, l_s is the specimen length, E_b is the Young's modulus of the bar, A_b is the cross-section area of the bar, and A_s is the cross-section area of the specimen.

1.3 Imaging Techniques and Computer Tomography

Beyond the averaged stress-strain response, recent advancements in simulation techniques of constitutive and fracture modeling have led to a desire for more detailed in-situ deformation information and fracture behavior. High-speed optical cameras [2] have been used to capture 2D deformation histories of transparent specimens and the surface structure of non-transparent specimens. Digital image correlation (DIC) techniques [8, 10] were integrated to Kolsky bar to obtain full-field strain measurements on the specimen surfaces. The conventional DIC is conducted via spraying speckle patterns onto specimen surface, and using software to track the movement of individual patterns. However, for non-transparent materials, this requires the assumption that the material deformation inside the specimen is exactly the same as the deformation on the surface, since the DIC method can only obtain surface information. Chen [9] used a synchrotron X-ray source and a high-speed camera with scintillator to image the specimen sub-surface damages loaded by a Kolsky bar. Due to the configuration of current synchrotrons, the specimen can only

be visualized in one direction during the dynamic loading. In nondestructive evaluation theory, the crack inside the specimen is sensitive to X-ray if it is parallel to the X-ray beam direction, but it is not detectable if it is perpendicular to the X-ray beam [20]. Thus, current high-speed imagining techniques are focused on the deformation of 2D specimens, where the thickness direction of the specimen is parallel to the light path (both visible light and X-ray).

However, most of compressive experiments require the specimen to be a 3D shape. For example, cylindrical specimen is usually used in uniaxial compression experiments to reduce the stress concentration effect. In such case, a researcher can only get a surface image by using a visible light high-speed camera, or a projection image from one angle by using synchrotron X-ray, which in both cases the cracks perpendicular to viewing direction are missed. To overcome this, one need an imaging system which is able to measure 3D information of the specimen.

Currently, there are two types of techniques that can obtain 3D measurements: 3D-DIC and computer tomography. Similar to conventional 2D-DIC, 3D-DIC also tracks the movement of speckle patterns on the specimen surface, but with two cameras from different angles [10]. However, 3D-DIC is still limited to surface features, and it will miss all the subsurface failures. Computer Tomography (or CT) is widely used in medical and industry applications to generate cross-sectional images in the radiation direction of a static object. Such cross-sectional images can then be connected to form a detailed inner 3D volume of the test subject. Conventional CT takes multiple 2D projections from different angles, via either rotating specimen or X-ray source, as shown in Figure 1.2. However, the time for this rotation movement takes from few seconds to few hours to complete. Thus, the conventional CT is not suitable to analysis in-situ Kolsky bar type impact event, which the loading duration is in the order of milliseconds to hundred microseconds.

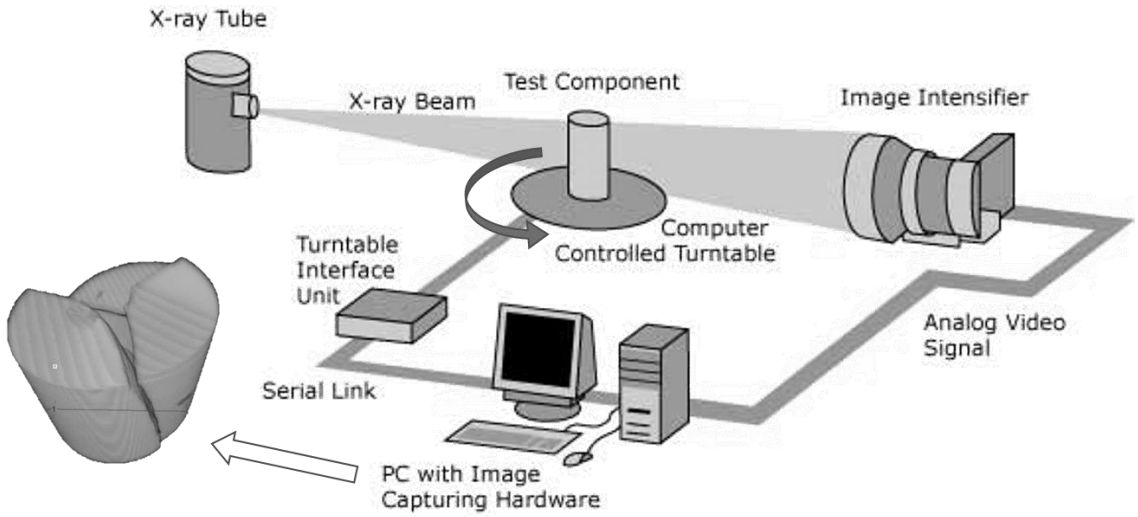

Figure 1.2 Schematic of conventional computer tomography [21].

It is noted that some researchers CT-scanned the deformed specimen or fractured pieces after the loading for post failure analysis [50, 51]. However, in such cases one has to consider the dynamic unloading due to the release of impact loading. Furthermore, in some circumstances, the specimen would fail catastrophically and leaves too many pieces, where it is very difficult to recover and interpret the debris.

1.4 Flash X-ray Tomography

Utilizing reconstruction algorithms developed for CT [15, 16, 17], a good candidate to obtain the dynamic in-situ 3D specimen sub-surface information is the multichannel flash X-ray, for its ability to take instantaneous projections from different angles. A flash X-ray system is usually used to imaging shock events, the application includes shock physics, bullet penetration events, and body armor and helmet protections [13]. It emits a pulsed X-ray radiation by high current discharging of a cold cathode X-ray tube from a large capacitor [22]. The duration of such pulse is in the order of 10 ns to 1 μs, which is short enough to image the dynamic events in-situ without the motion blur. Chen [23] used flash X-ray with gas gun to monitor the motion of high-speed projectile shooting into a granular target in dynamic penetration experiments. Fugelso [24] also used flash X-ray to image a mockup PBX cylinder striking a steel plate and estimated the density distribution of the projectile during the impact.

Traditionally, multichannel flash X-ray was used to take multiple 2D projections at different time during the same event. By taking 2D projections at the same time from different angles, one can reconstruct the 2D projections to 3D volume data of the specimen without the rotation movement mentioned in last section. Meanwhile, the triggering time of the X-ray flash can be precisely controlled and synchronized with the Kolsky bar strain gage signal, which leads to that the reconstructed volume information can be tracked in terms of specimen stress-strain.

To author's knowledge, no 3D in-situ Flash X-ray tomography for Kolsky bar experiments has been previously conducted yet. However, there are few researches who have conducted to use multichannel Flash X-ray to do tomography for penetration events. Lin [25] used two orthogonal flash X-ray sources to imaging the gelatin cavity induced by ballistic penetration, and approximated the outer surface of the cavity by B-spline elliptic approximation of the edge detection of the original 2D projections. However, the volume information inside the cavity was not obtained. Zoltani [11] used 21 flash X-ray heads to image a 16.5-cm-diameter phantom and reconstruct its cross-section by maximum entropy algorithm, where the resulting spatial resolution was 2 mm. Recently, Moser [12] used 6 flash X-ray heads (5 in-plane and 1 out-of-plane) to image ballistic penetration on a 15-by-15 cm ceramic plate and reconstruct by MART algorithm, where the debris distribution was clearly obtained via a spatial resolution of ~1 mm. As shown in Figure 1.3 for the experimental setup from Zoltani [11], the distance from specimen to X-ray source is 2.1 m and the distance from specimen to detector is 1.68 m. However, in the nondestructive evaluation applications, it is desired to minimize the distance from specimen to detector for a better geometric unsharpness [20].

The geometric unsharpness is the image blur induced by finite size of the focal spot of the X-ray source (comparing to an infinite small point source). The specimen can be exposed by the X-ray emitted from any point of the focal spot and resulting a penumbra on the imaging plane (as shown in Figure 1.4). The size of such penumbra U_g can be written as

$$U_g = \frac{fb}{a} \tag{1.4}$$

where the f is the size of the X-ray source focal spot, a is the distance from source to specimen, and b is the distance from specimen to detector. Thus, to reduce the geometric unsharpness for a given type of X-ray source type, one can 1) increase the source-specimen distance or 2) decrease the specimen-detector distance. However, increasing the source-specimen distance would reduce

the X-ray photon density of the image and resulting a higher noise ratio when digitizing the projection image; and decreasing the specimen-detector distance might lead to the interference between each channel (which means the detector might be exposed by more than one channel of X-ray).

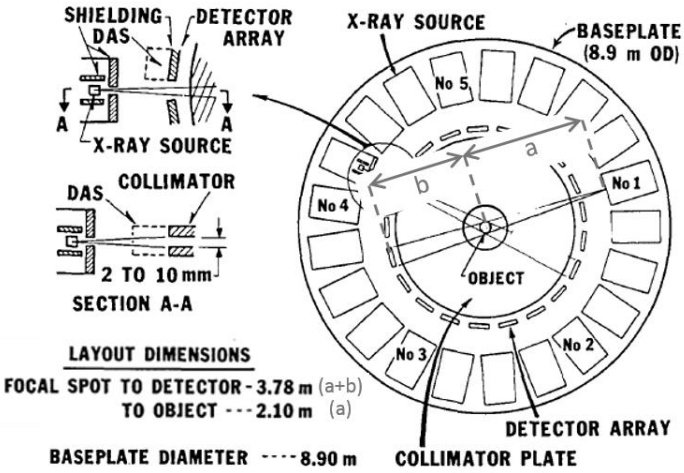

Figure 1.3 Multichannel flash X-ray setup from Zoltani *et al.* [11] showing the distance from specimen to X-ray source is in the same order of magnitude with the distance from specimen to detector.

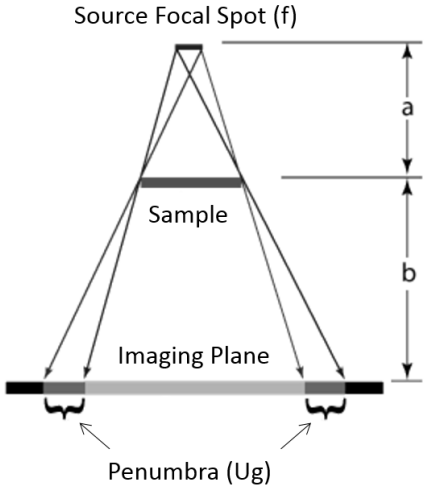

Figure 1.4 Illustration of geometric unsharpness.

The geometric unsharpness of the setup from Zoltani [11] is range from 1.6-4 mm, while the geometric unsharpness from Moser [12] is about 1 mm. Such geometric unsharpness is probably

good enough for the penetration specimens in the literatures where the specimen size is about 15 cm, but not suitable for Kolsky-bar-type specimens where the common diameters are in the range of 1 – 20 mm. On the other hand, the datasets of penetration debris are sparse. The sparse dataset means that majority of the voxel values are zero in the 3D reconstructed volume, such as the reconstruction of ballistic penetration fragments distribution [12], where the distance between nearest neighboring fragments is at least in the same order of fragment size. A counterexample is the Kolsky bar specimen failure process [2]. The majority of the fractured specimen is still close to each other (reconstructed volume is dense), where the distance between neighboring fragments is much smaller than the fragment size. Sparse reconstructions from limited number of projections were less difficult than dense datasets such as the cracks inside the Kolsky bar specimen.

1.5 Summary

The Kolsky bar technique enables accurate loading and measurement of the specimen response at dynamic deformation rates. Dynamic in-situ 3D specimen volume information is in critical needs for dynamic fracture analysis and modeling. Due to the limitations of high deformation speeds, relatively small specimen sizes and dense datasets, it is difficult for existing methods to obtain practical in-situ volume images of the specimen.

In this research, the author designed a modified 4-channel flash X-ray system to take 2D projections from different angles and reconstructed the volume information with iterative reconstruction method to analyze Kolsky bar specimen fracture process. Two unique features of the current method are: 1) precise and repeatable control over the loading history of the specimen and the X-ray projection time, thus a correlation between the stress-strain/force-displacement response and the reconstructed volume can be clearly defined; and 2) low geometric unsharpness to improve reconstruction resolution by placing X-ray detectors close to the specimen without interference from unnecessary exposures.

A limitation of this method is that only one 3D reconstruction is available for each specimen, due to the fact that each flash X-ray head can only fire once during one measurement; thus real-time 4D volume-time information is not achievable. However, this can be relaxed by deforming identical specimens under identical conditions and firing X-ray at different specimen deformations.

In the next chapter, a detailed flash X-ray system design, construction and operation procedures are described. The imaging processing techniques and reconstruction algorithm are also discussed.

CHAPTER 2. METHODOLOGY

2.1 Concept Design

In this research, four flash X-ray heads are used. As shown in Figure 2.1, all four X-ray beams are in one plane and are 72-deg to the nearest neighboring beams, the specimen and the loading axis of the Kolsky bar pass through the conjunction of four X-ray beams. Out-of-plane X-ray beams are not selected as they would be blocked by the Kolsky bar itself. In this way, the angle between detector to specimen path and its neighboring X-ray source to specimen path is 36-deg (as shown in Figure 2.2). As discussed in previous chapter, to minimize the geometric unsharpness of the 2D projection for a given type of X-ray source, one should 1) place the X-ray head relatively far away from the specimen but still let enough X-ray photon to expose the specimen, and 2) place the detector as close as possible but without being double-exposed by non-relevant channels. In the current experimental setup, the source-to-object distance is 1.02 m and the detector-to-object distance is 50.8 mm. The focal spot size of the flash X-ray head used in this research is 3 mm. The resulting geometric unsharpness calculated from equation-1.4 is 0.15 mm.

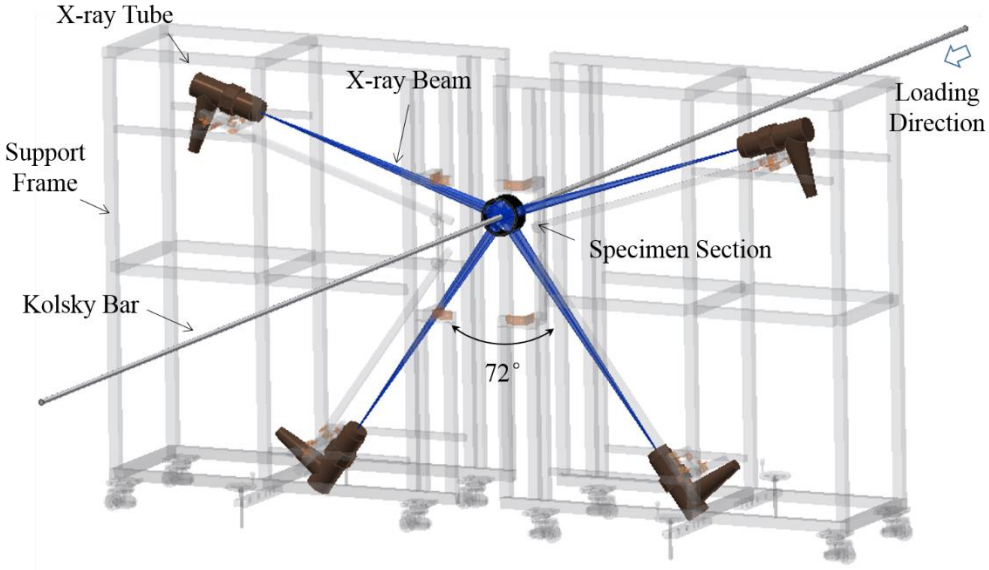

Figure 2.1 CAD schematic of modified flash X-ray setup.

Shown in Figure 2.2, a 6.35-mm-thick lead tube is installed behind detectors to block exposures from other channels. Four rectangular pockets are opened on the lead tube to serve as the aperture by letting the corresponding X-ray beam pass through. ScanX phosphor storage plates (PSPs) [26] were selected as the detectors. The size of the rectangular pocket is dependent on the detector size, where the detector size is dependent on the specimen size. In general, for a smaller size of specimen, it is possible to use a smaller size of open pocket size and a smaller size of detector, which one can select a closer detector-to-object distance and outperform a better geometric unsharpness. In this research, based on the diameter of Kolsky bar of 19.05 mm and availability of the commercial digitizable X-ray detectors, standard intraoral film size #2 is selected with a width of 31 mm and a length of 41 mm. Thus, the open pockets are machined to a width of 29.5 mm and a length of 43 mm. It is noted that the width of the pocket is calculated via the similar triangles from the width of the film and the detector-to-source distance; while the length of the pocket is set to slightly larger than the length of the film to ensure a full coverage of the desired X-ray exposure.

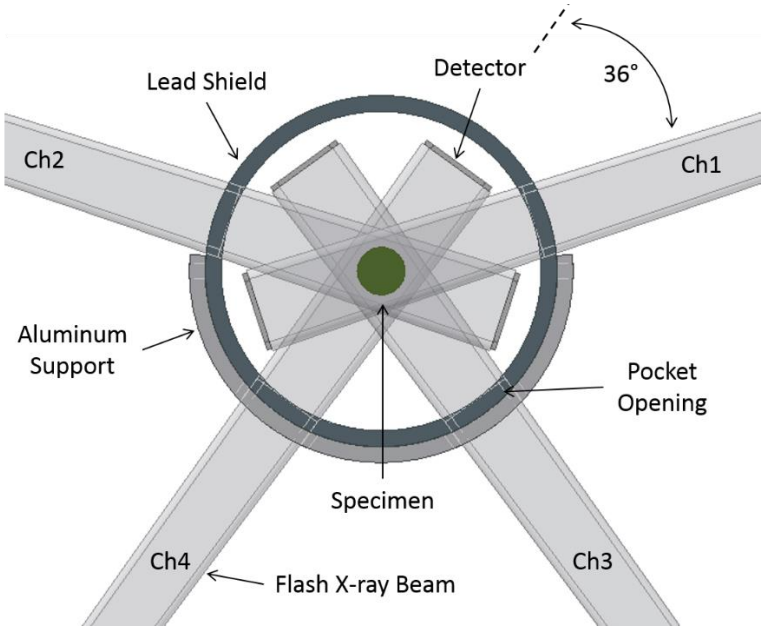

Figure 2.2 CAD schematic of specimen section in the modified flash X-ray setup.

2.2 Construction of Experimental Setups

The X-ray heads are mounted on two moveable T-slot frames, which are covered by 3.2-mm-thick lead-lined plywood to protect the operating personnel from excessive radiation exposure. The

moveable design reduces the difficulty to replace consumable equipment such as X-ray tubes and connecting cables. Figure 2.3(a) shows a photo of the T-slot frames taken before covering the lead plywood. The red arrows indicate the approximate location of the four X-ray heads. Figure 2.3(b) shows a side view photo inside the frame. The right-angle blue-colored blocks are the flash X-ray heads, and the green line is the indication of a line laser mounted on one of the frames, which was used to align the location of X-ray heads and the specimen. Since the frame is moveable, the line laser was also used to quick-align the relative location of the two frames by pointing to an indicator mounted on the other frame.

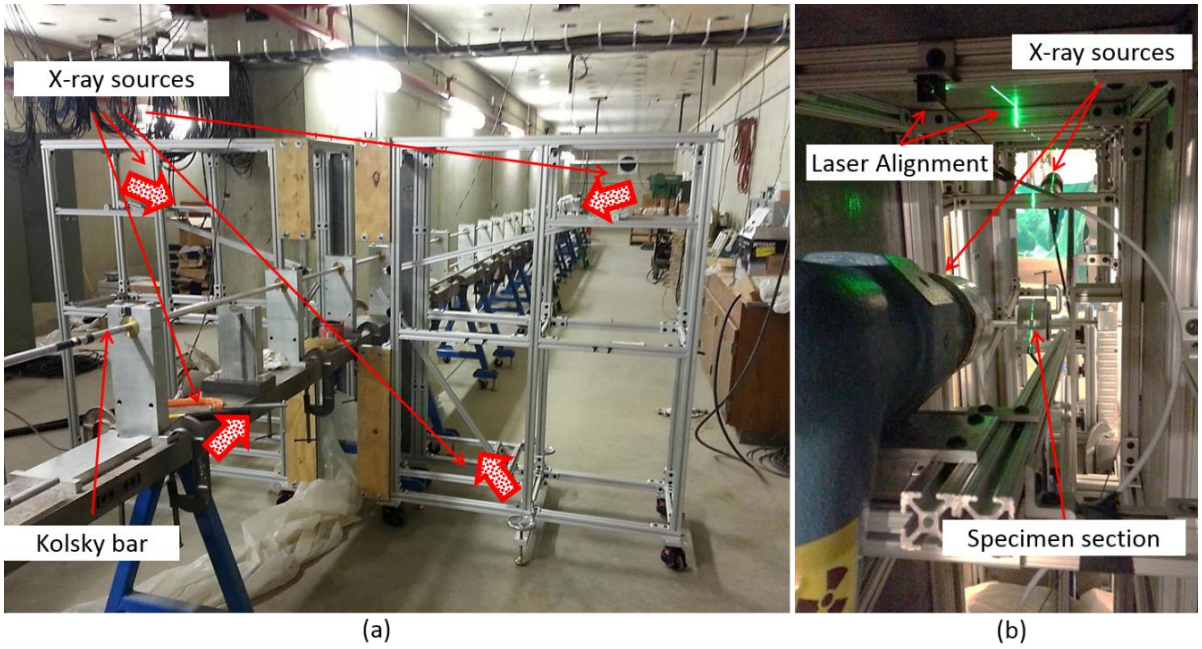

Figure 2.3 Photos of modified flash X-ray setup showing (a) front view of the framework to support the 4 flash X-ray heads, and (b) side view inside the frame with mounted flash X-ray heads, line laser for alignment and specimen section.

Figure 2.4(a) shows a front-view photo of the specimen section. As aforementioned, a lead tube with four pocket opening is used to block undesired X-ray radiation. Due to the low stiffness of lead, where it might deform under its own weight overtime, such lead tube was installed on a half-circular shaped aluminum support, and the aluminum support is mounted on an adjustable frame to align the location of the lead tube. Inside the lead tube, a 3D-printed fixture (details shown in Figure 2.5(a)) is used to hold the X-ray detector assemblies (details shown in Figure 2.6). A dust

cover which is made of thin printing paper surrounds the specimen to retrieve the debris of fractured specimen and to reduce dust contamination of X-ray detectors. Due to the thin-thickness and low-density of the paper, it is transparent for the X-ray used in current research. Figure 2.4(b) shows a photo taken through the open pocket, where the green line is the light reflection from the alignment line laser, which indicates the center of X-ray beam and the detector.

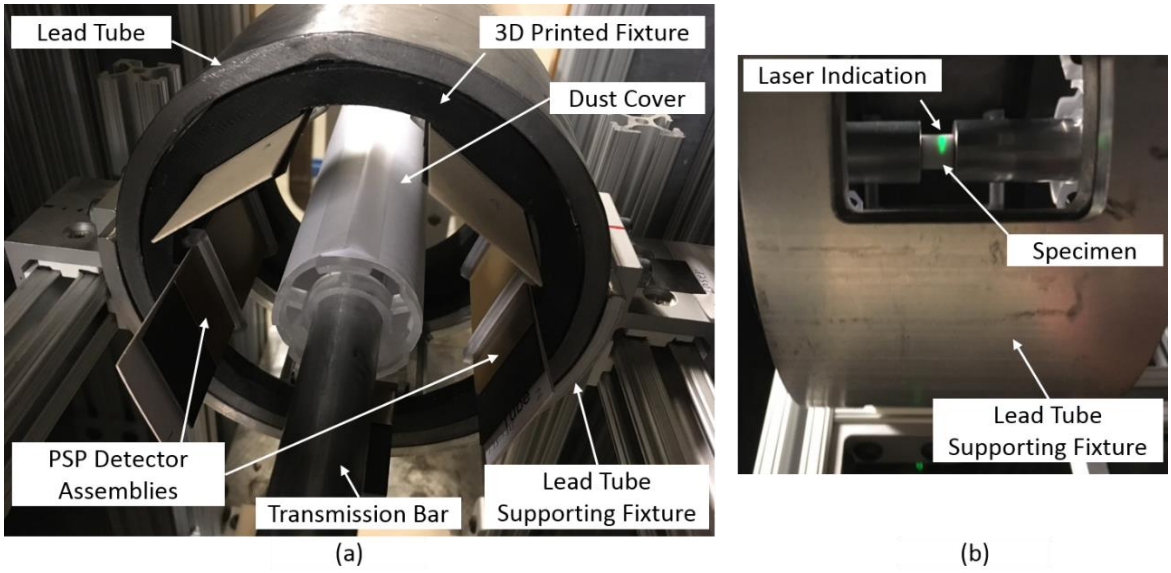

Figure 2.4 Photos of specimen section: (a) front view showing the assembly, and (b) side view passing through the pocket opening of the lead tube.

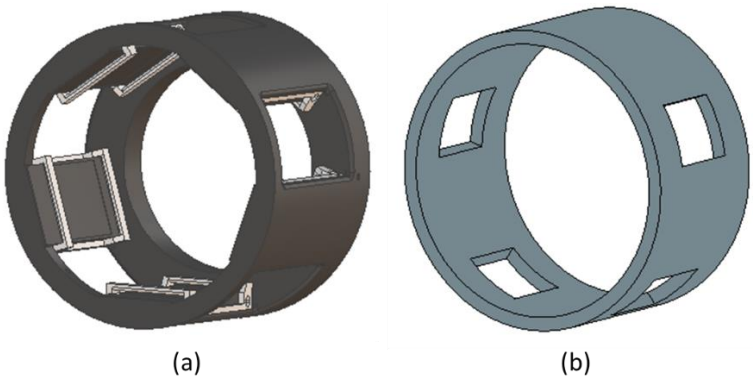

Figure 2.5 CAD models of (a) the 3D printed fixture inside the lead tube used to hold PSP assemblies, and (b) the lead tube with four pocket openings.

Figure 2.5(a) shows the CAD model of the 3D printed fixture to hold detectors in place. The detector assembly can be tight-fitted into the slots between pocket openings on the outer surface. The dimensions are carefully adjusted so that the 3D printed fixture would not block any X-ray beam passed from the openings of the lead tube. Due the angle of 72-deg between each channel, the maximum number of detectors can be fitted is five. In this research, four out of five detectors are aligned to the four directions of X-ray beam, and the remaining one is intentionally placed without being in the path of any X-ray beam. The purpose of the unexposed detector is to measure the dark current due to non-perfect shielding of the lead tube. Figure 2.5(b) shows the CAD model of the lead tube which is placed outside the 3D printed fixture with only four openings, which are aligned with the X-ray beam directions.

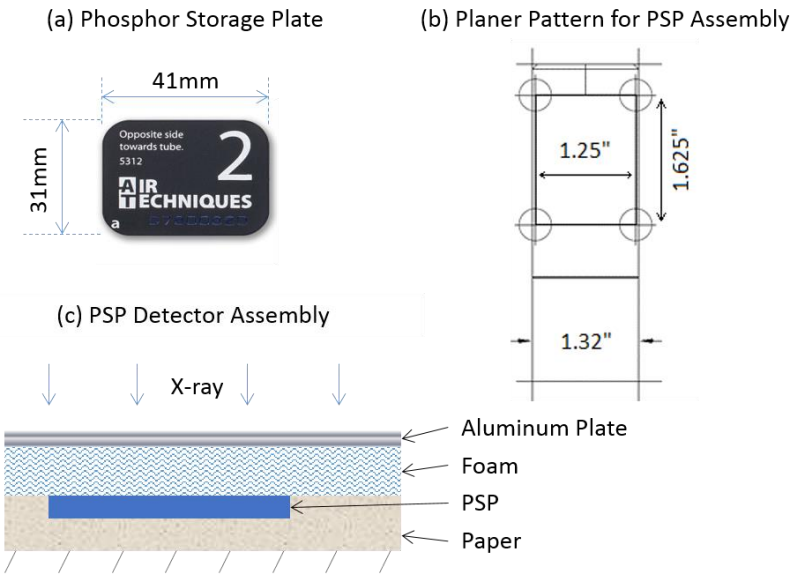

Figure 2.6 Phosphor storage plate (PSP) assembly: (a) photo of a standard intraoral size #2 ScanX phosphor storage plate from air techniques [26], (b) planer pattern used to cut the paper base for the PSP assembly, and (c) cross-section schematic showing each layer of the assembly.

Figure 2.6 shows the phosphor storage plate (PSP) used in this research and the assembly for PSP protection and easy handling. The thickness of the PSP is about 0.5 mm. For a good imaging quality and reduce the potential scratches of the PSP plate, it is desired to place the PSP in a closed environment away from dust, hard objects, and grease from human hand. In this research, the PSP is sandwiched between a cardboard paper sub-assembly layer on the back and a micro-cell foam layer on the front (as shown in Figure 2.6(c)). A thin layer of aluminum is placed on top of the

foam to filter the scattered or cross-scattered low energy X-ray photons and protect detectors from high-speed debris which penetrates dust cover during the dynamic loading. The cardboard paper sub-assembly is also used to constrain the lateral movement of the PSP in the directions perpendicular to X-ray beam. To make such cardboard paper sub-assembly into desired shape: a first layer of printable cardboard paper is printed into the pattern indicated in Figure 2.6(b); then it is glued onto a second layer of same paper; after drying, the rectangular slot of 1.25" (31.75mm) by 1.625" (41.28mm) is cut via razor blade from the glued two layer; the remaining is again glued onto a third layer of cardboard; and finally the paper sub-assembly (with a width of 1.32") is cut via a desktop paper trimmer. The thickness of each individual cardboard layer is ~0.22 mm. The final assembly is chamfered on edges for the ease to insert into the slot of 3D printed fixture.

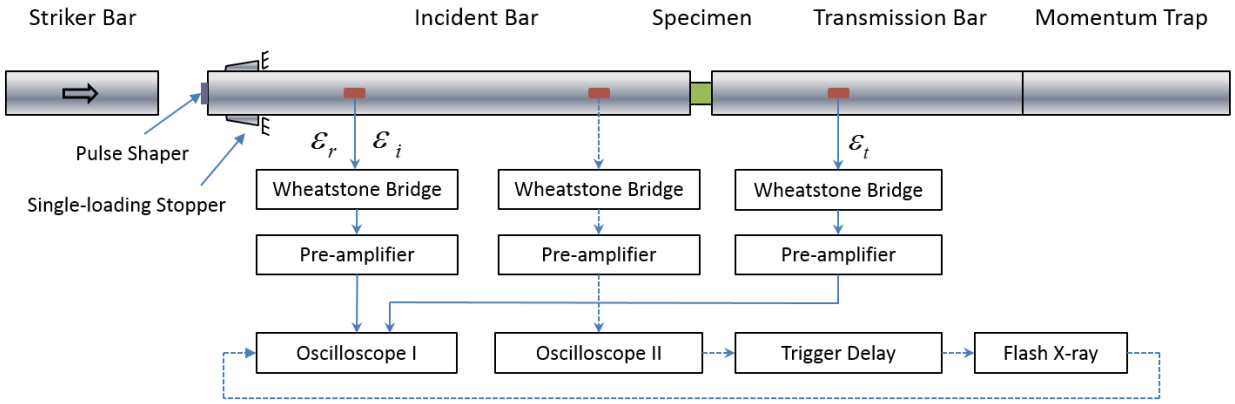

Figure 2.7 Schematic of modified Kolsky bar setup for flash X-ray system.

A modified Kolsky compression bar setup was used to load the specimen. As shown in Figure 2.7, the compression setup consists of a striker bar, an incident bar, a transmission bar and a momentum trap. All bars shared a common diameter of 19.05 mm and were pre-aligned to a same axis. The material of all bars is aluminum 7075-T6. The lengths of the striker, incident bar, transmission bar, and momentum trap are 1.22 m, 10.97 m, 7.32 m, and 3.67 m, respectively. A pulse shaper attached on impact end of incident bar was used to reduce high frequency oscillations and shape the incident pulse. A single loading stopper was clamped on incident bar to prevent the specimen from multiple loading induced by wave reflections inside the incident bar. Three pairs of strain gages were attached on the bars: a pair on incident bar to record the incident and reflected pulses; a pair on transmission bar to record the transmission pulse; and a pair on incident bar towards the specimen

end to trigger the flash X-ray. A Model 43731A flash X-ray system from L-3 communications was used in this research. In the system, four 150 kV flash X-ray tubes were installed, which allow exposure time as short as 70 nanoseconds [13]. It is note that the 150 kV is the nominal voltage of the tube. The generated X-ray is white beam where the spectrum is a continuous function from zero to 150 keV. In a measurement, the striker bar is fired by a gas gun to a desired speed. The striker bar impacts pulse shaper and deforms the pulse shaper to generate an incident wave, which is recorded by oscilloscope I when propagating along the bar and triggers the oscilloscope II. The oscilloscope II features a trigger output function. When the voltage was above certain level, it generated a rectangular pulse to trigger the delay amplifier. After a pre-set delay time, the flash X-ray was triggered and fires X-ray beam towards the specimen. The delay was set to the summation of the intended delay position in the stress-strain and the delay time due to wave propagation from the triggering strain gage to the bar end, minus the rising time of the incident wave from zero to the triggering voltage. In this way, one can synchronize the flash X-ray with the Kolsky bar and correlate the 2D projections and/or 3D reconstructed volume to the specimen stress-strain.

2.3 Operation of the System

As mentioned earlier, it is desired to deform the specimen under a constant strain rate to effectively delineate rate dependency of the material behavior. During a Kolsky bar experiment, the strain rate is proportional to the reflected pulse (equation 1.1). To achieve a relatively constant strain rate, pulse shapers are used to shape the incident pulse for a flat reflected pulse [4]. Several trial-and-errors are iterated to find the best combination of pulse shaper material, diameter, thickness, and striker speed for a desired strain rate condition. The bar locations and the rigid end of the single loading stopping mechanism (in Figure 2.7) are adjusted according to the specimen thickness to ensure the initial position of the specimen is aligned with the center of the X-ray beams (Figure 2.4(b)). The gap between the single loading stopper and the rigid end is adjusted based on striker length and striking velocity to prevent multiple loadings of the specimen.

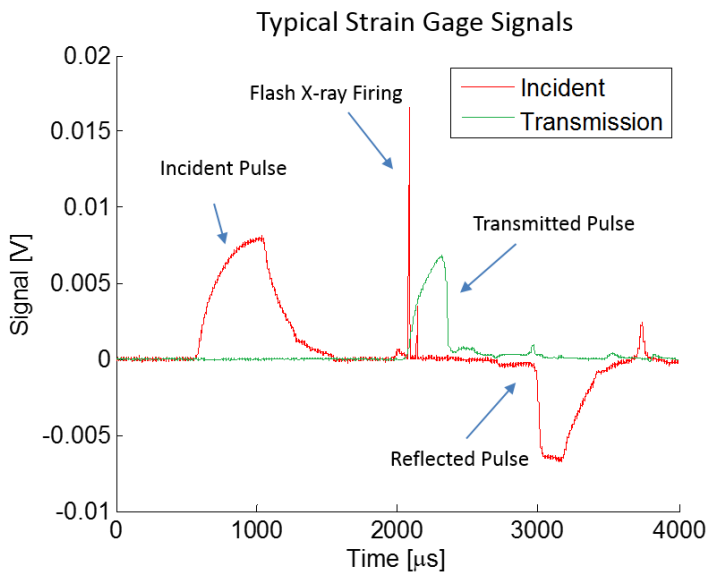

Figure 2.8 Typical raw signals from strain gages on incident bar and transmission bar.

Figure 2.8 shows a typical raw strain gage signals without any filtering. The bi-linear shape pulse from ~550 μs to ~1050 μs is the rising-edge potion of the incident pulse which was generated by a pulse shaper; the pulse from ~2050 μs to ~2350 μs in transmission channel is the transmitted pulse, which shows a sudden drop at ~2350 μs indicating a brittle failure of the specimen; and the pulse from ~2700 μs to ~3200 μs in incident channel is the rising potion of the reflected pulse, where the flat potion from ~2700 μs to ~3000 μs indicates the specimen was under a constant rate deformation before the breakage. The sharp spike at ~2100 μs aligns with the time when flash X-ray was fired. It is assumed that this sharp spike is due the electrical-magnetic field induced by the 2 kA discharge current from flash X-ray pulsers to flash X-ray tubes. The duration of such spike is 13±0.5 μs, and it is consistent across all the experiments. It is noted that this spike is smoothed out during stress-strain calculation by linear interpolating the data points before and after the spike.

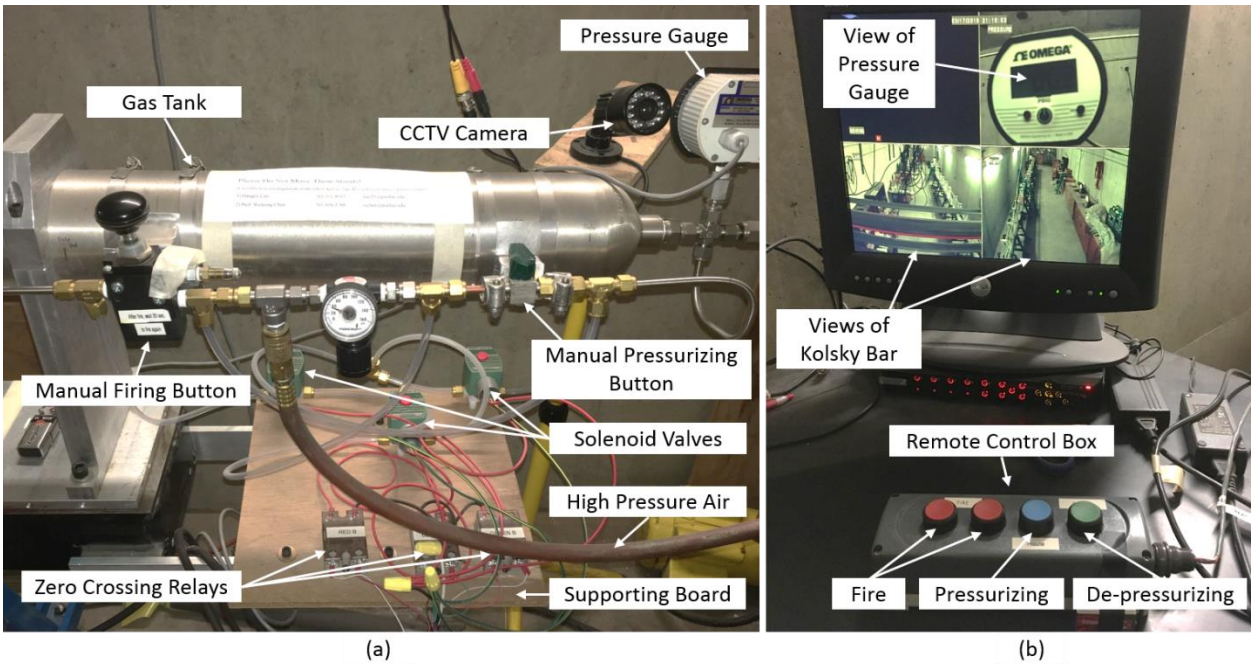

Figure 2.9 Photos of gas gun remote firing system: (a) wiring of solenoid valves and manual firing system, and (b) remote control box and CCTV camera views.

Excessive X-ray radiation is harmful to human body. To protect the operating personnel and reduce the exposure from X-ray radiation, it is desired to keep the personnel as far as possible and/or with as many as possible protections. In this research, the personnel are not allowed to stand in the lines where the X-ray heads are pointing to, due to the high instantaneous intensity of the flash X-ray system. The closest personnel stand obliquely behind a 3.2-mm-thick lead shielding and a ~0.6-m-thick concrete wall, with a shortest oblique distance to the X-ray source of about 4 m. The measured doses at the personnel position is less than 10 μ-rem per shot (by Purdue Radiological and Environmental Management team). As a comparison, the common standard for radiation worker annual does limit from Code of Federal Regulations is 5 rem [27]. However, the gas gun section of the Kolsky bar is exposed to the scattered radiation. In this research, a remote firing system was built for the gas gun, as shown in Figure 2.9. Operating in parallel to the manual firing system, three zero crossing relays controls three solenoid valves for the action of firing, pressurizing the tank, and depressurizing the tank, respectively. The zero-crossing relay reduces the electric noise during the on-off operation comparing to traditional mechanical relays. A CCTV camera is used to monitor the pressure in the tank. To avoid firing the striker accidentally, two

firing buttons were designed on the remote-control box, where both buttons need to be pressed to fire the striker.

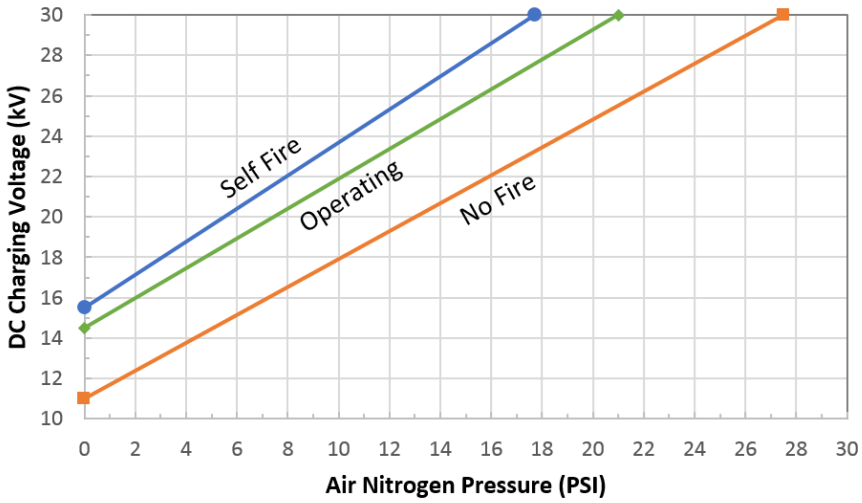

Figure 2.10 A photocopy of nitrogen pressure vs charging voltage of the flash X-ray pulser.

The flash X-ray pulsers are filled with dried nitrogen (or dried air) to operate. Pressure too high would result in no-fire, while pressure too low would lead to self-fire during the charging process. The preferred pressure of the nitrogen is linearly related to the charging voltage (as shown in Figure 2.10). In this research, the charging voltage is set to 28 kV for a nearly maximum X-ray intensity output with a balanced flash X-ray tube life, and the resulting nitrogen pressure is set to 18.3 psi. To scan the stored 2D images from the PSPs, a ScanX-14 digital imaging system [26] is used to digitize the projections and reset the PSPs for next-time use. The 2D spatial resolution from such digitizing system is 0.05 mm/pixel. The ScanX-14 was originally designed for large size PSPs. To scan intraoral size PSPs, a carboard holder was made to feed the intraoral size PSP into a desired depth. It is found that to start the scanning process, the intraoral size PSPs need to be feed under the green indication light position (as shown in Figure 2.11). It is suspected that the ScanX-14 only has limited number of PSP detectors, and the machine only starts the full-field digitizing after one of the detector detects the PSP. It is noted that before the first experiment of the day, the PSP detectors need to reset by passing through the ScanX, since the detectors will be gradually exposed by environmental radiation over time.

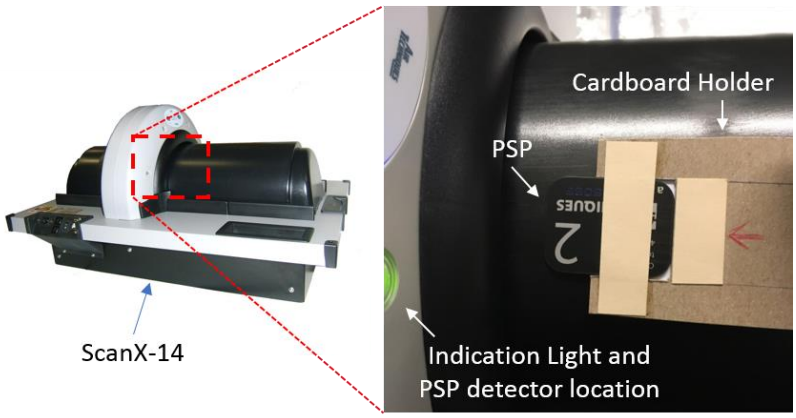

Figure 2.11 Using ScanX-14 to scan intraoral size PSPs.

2.4 Image Processing Techniques and Typical 2-D Projections

The PSP detector is advertised to outperform traditional film-based detectors for the linearity over a wide exposure range [26]. In this research, two aluminum step-shaped blocks were machined to calibrate the sensitometry and linearity of the PSP. As shown in figure 2.12(a), the thickness of the first block increases from 10 mm to 18 mm with an increment of 2 mm per step. Similarly, the thickness of second block increases from 2 mm to 10 mm in 5 steps. The color bar on the right shows the greyscale value of the raw images. In these raw images, lighter areas indicate higher photon intensity in the detector, which the incoming intensity is less attenuated. By taking the ratio between averaged greyscale value of each block to the surrounding white background (non-object exposure value), the penetration ratio (I/I_0) of the aluminum block for the PSP detector signal is obtained (as shown in Figure 2.12(b)). It is noted that the I/I_0 is plotted in log scale. For a specimen with a same type of material, the I/I_0 can be calculated based the material X-ray attenuation coefficient μ:

$$\frac{I}{I_0} = e^{-(\mu x)} \tag{2.1}$$

where the *x* is the thickness in the X-ray beam direction. It is noted that the attenuation coefficient is a variable with respect to X-ray photon energy, and the energy spectrum from flash X-ray output is a continuous function from 0 to 150 keV [13]. In the sensitometry calibration, the material is the same across the specimen. Thus, the effective attenuation coefficient is constant, leaving the only

variable of thickness. In Figure 2.12(b), it is found that the until a thickness of 14 mm, the PSP response is very linear. The half-penetration depth is found to be 10.4 mm. By comparing the mass attenuation coefficient data of aluminum [28], the effective X-ray photon energy is found to be around 68 keV.

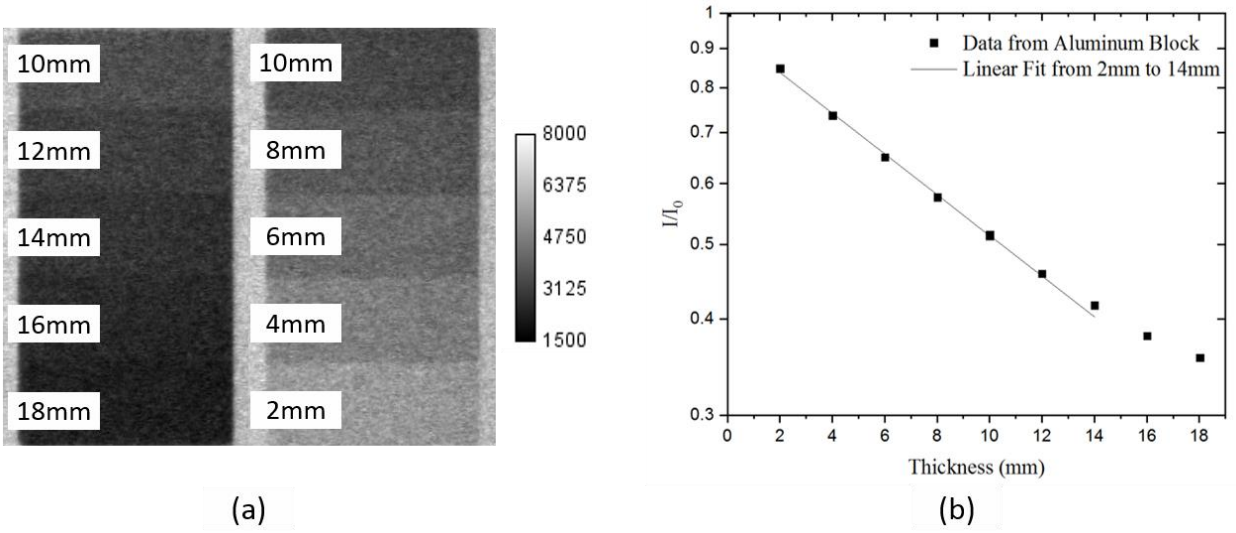

Figure 2.12 Verify the linearity of the PSP detector: (a) 2D images of aluminum calibration blocks, and (b) detector sensitometry - the greyscale ratio of aluminum block to white background in detector signal verses the thickness of the aluminum block.

Alignment process of acquired images was needed, since for each measurement the PSPs were manually inserted to digitizing system which might induce unnecessary rotation and translation. As shown in Figure 2.13, edge detection was performed firstly for raw image to detect the position of the bars. Such algorithm was accomplished by Canny method [14] incorporated in MATLAB image processing toolbox. After the angle of bar axis was corrected to vertical, the center position of the specimen was obtained by averaging the x & y positions of bars' boundaries. Based on the angle, center information and a width & height of intended reconstruction area, the projection was cropped so that the rotation axis for reconstruction was in the center of the cropped image. The accuracy of this alignment method is within 1-2 pixels. For some experiments, the cropped projection during deformation was normalized with respect to its un-deformed state of corresponding channel based on equation 2.2-a. For the other experiments, direct input was used

as shown in equation 2.2-b. For some reconstruction algorithms a weight function is required, which is shown in equation 2.3.

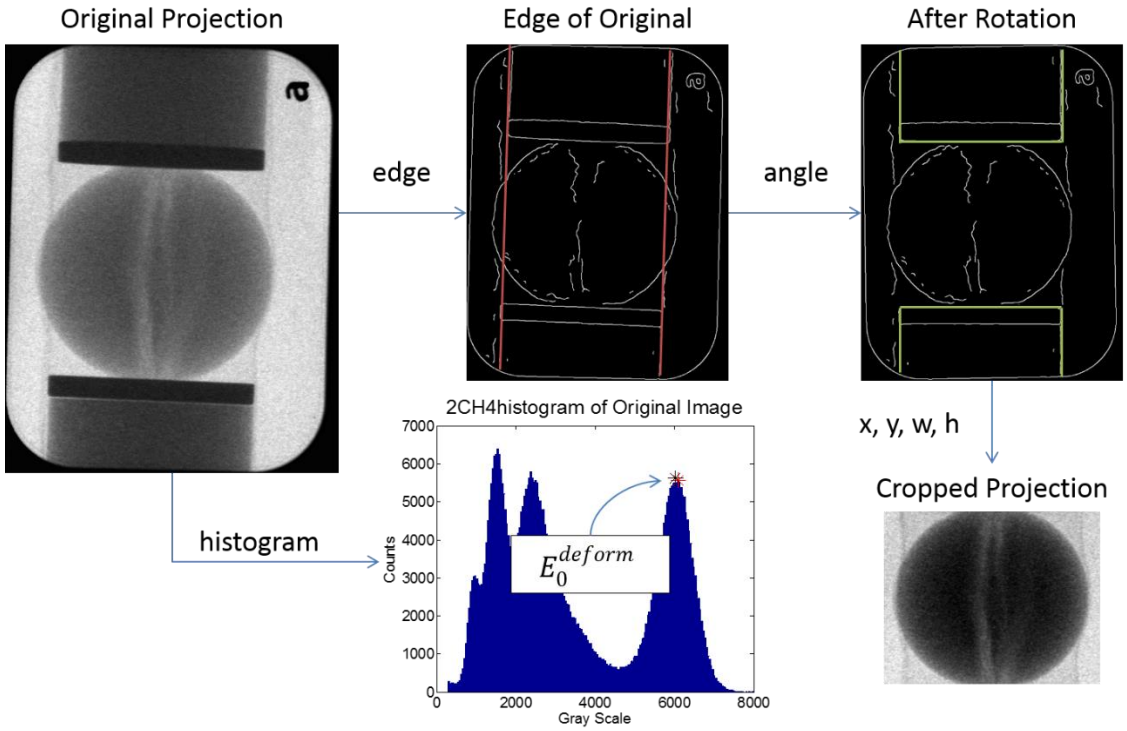

Figure 2.13 Image alignment procedures.

$$input = \ln\left(\frac{E_0^{undeform} - E_{dark}}{E_x^{undeform} - E_{dark}}\right) - \ln\left(\frac{E_0^{deform} - E_{dark}}{E_x^{deform} - E_{dark}}\right) \quad (2.2\text{-a})$$

$$input = \ln\left(\frac{E_0^{deform} - E_{dark}}{E_x^{deform} - E_{dark}}\right) \quad (2.2\text{-b})$$

$$weight = \left|\left(\frac{E_0^{undeform} - E_{dark}}{E_x^{undeform} - E_{dark}}\right) - \left(\frac{E_0^{deform} - E_{dark}}{E_x^{deform} - E_{dark}}\right)\right| \quad (2.3)$$

where $E_0^{undeform}$, E_0^{deform}, $E_x^{undeform}$, E_x^{deform}, and E_{dark} are the non-object exposure from undeformed state, non-object exposure during deformation, aligned projection from un-deformed state, aligned projection during deformation, and dark current exposure, respectively. The non-object exposure is the grey value in an image that represent the exposure of incoming X-ray beam without the attenuation of any object, which is equivalent to the mean value of the white area in the projection. In practice, it was approximated by finding the gray value where it has the

maximum counts of the brightest Gaussian peak in the histogram of the projection (Figure 2.13). The dark current is the grey value that represent the image without main X-ray beam exposure. In this study, the dark current was calibrated from the 5th channel detector mentioned earlier which is located not in the path of any X-ray beams (Figure 2.5(a)). The dark current value for each channel (1-4) is calculated by the average grey value of the 5th channel (${E_0}^{(5)}$), divided by the sum of non-object exposure from all four channels ($\sum_{j=1}^{4} {E_0}^{(j)}$), and times the sum of non-object exposure from other three channels ($\sum_{k=1}^{4} {E_0}^{(k)} - {E_0}^{(i)}$):

$$ {E_{dark}}^{(i)} = \frac{{E_0}^{(5)} \times (\sum_{k=1}^{4} {E_0}^{(k)} - {E_0}^{(i)})}{\sum_{j=1}^{4} {E_0}^{(j)}} \tag{2.4} $$

Figure 2.14 shows a typical set of input and weight images. The projection of undeformed specimen is processed by a small radius median filter to reduce the noise in the reconstruction. The log input is the image input directly for tomography reconstruction algorithm. In the input image, the white area represents the cracked volume where the deformed state has lower density than un-deformed state; while the black area represents the expanded volume where the deformed state has higher density. The weight is an add-on term that marks the importance of each part of the image. Higher difference between deformed and un-deformed state leads to higher weight, which were visualized as the white area.

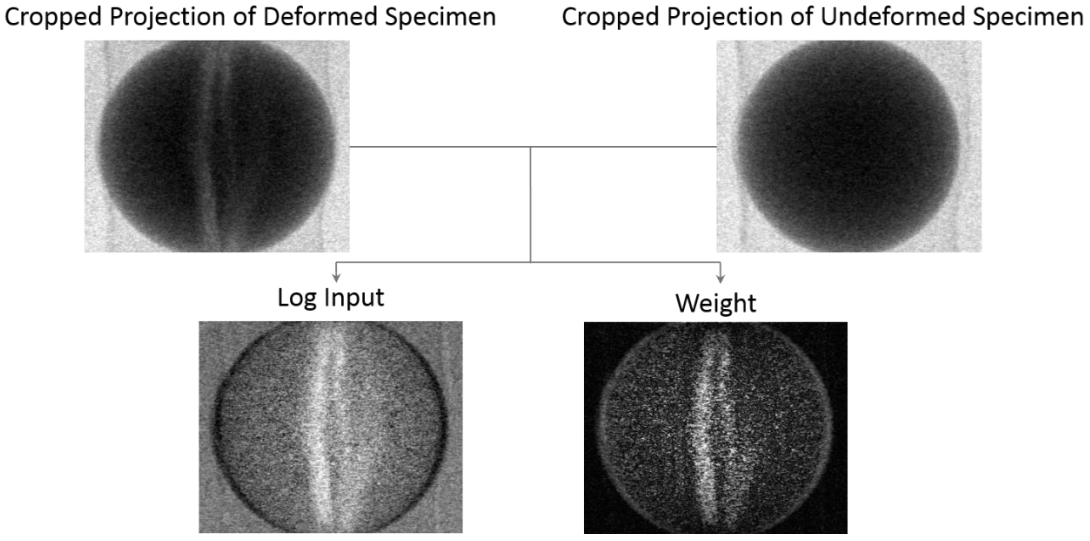

Figure 2.14 A typical set of log input and weight images.

2.5 Tomography Reconstruction Technique

Due to the limited number of projections, it is desired to use iterative reconstruction algorithms as comparing to traditional filtered back projection method [30, 31]. The algebraic reconstruction technique (ART) [29] is used in this research. The ART method is implemented by sequentially updating reconstructed volume by comparing the real projections to the virtual projections projected from the reconstructed volume. This method is incorporated within tomoj plug-in of the ImageJ software [15], which can be expressed in Equation 2.5-2.8.

$$\rho_j^{q+1} = \rho_j^q + \sum_i \lambda \, w_{i,j} \frac{R_i - R_i^q}{N_i} \tag{2.5}$$

$$N_i = \sum_j {w_{i,j}}^2 \tag{2.6}$$

$$R_i^q = \sum_j w_{i,j} \rho_j^q \tag{2.7}$$

$$\rho_j^0 = \frac{\sum_i R_i}{n} \tag{2.8}$$

where ρ_j^q is the X-ray density of a reconstructed voxel j at q-th iteration, ρ_j^0 is the initial guess and the starting point of the reconstruction, $w_{i,j}$ is the weight between projection pixel i and voxel j, R_i is the real projection obtained from the experiment, R_i^q is the q-th iteration virtual projection projected from ρ_j^q, n is the total number of voxels, and λ is a relaxation parameter to reduce the noise.

To start the algorithm, equation 2.8 gives an initial guess for the reconstruction volume, where each voxel is assigned to the average value from the sum of projection pixel values. Then each voxel value is updated based on equation 2.5 for each iteration. It is noted that the weight matrix $w_{i,j}$ represent the relationship between each voxel in the reconstructed volume and each pixel in projections. Such weight matrix is sparse, and the size of such weight matrix is very large. For example, the matrix $w_{i,j}$ for a 3D 200^3 volume projects to four 200^2 planes has about $1.28*10^{12}$ elements, which might take ~10 TB storage space for double precision. Thus, it is not computational practical to pre-calculate and store such matrix and perform linear algebra calculation to update the volume at once for each iteration. Instead, it is desirable to calculate the

weight when needed, which means the weight is calculated for each voxel-pixel pair for each single update. Such process involves multilevel computational loops. Currently this process is typically programed in C/C++, especially for 3D reconstructions.

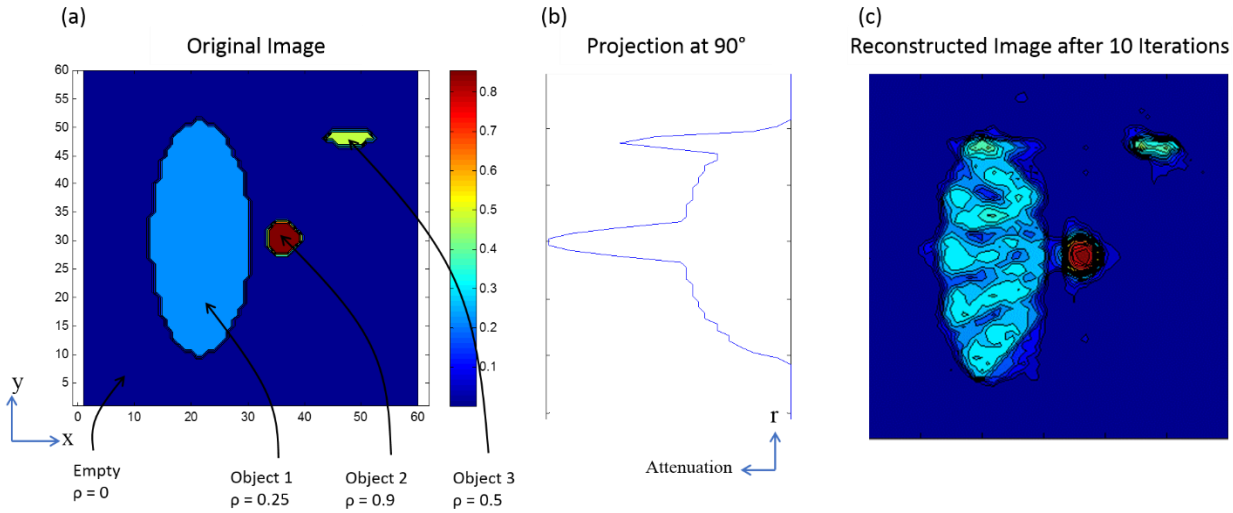

Figure 2.15 Simulated ART reconstruction of planar ART reconstruction of a simulated phantom containing three different ellipses: (a) original image, (b) a projection at 90-deg, and (c) reconstructed image after 10 iterations.

To illustrate the reconstruction process, two trial reconstructions were conducted by simulating reconstruction of a 2D image from few 1D projections. A first trial 2D planar phantom (60-by-60 pixel) was simulated as shown in Figure 2.15(a). The simulated phantom contains three ellipses with different geometries and densities (in the range of 0-1, as shown in the color bar next to the image). Figure 2.15(b) shows a projection image (in terms of attenuation) from 90-deg to y-axis, where high attenuation indicates higher value in the material density line integral of the X-ray beam path. The weight $w_{i,j}$ is calculated based on linear interpolation of nearest voxel values to the line integration points. Eight 1D projections were generated by linear interpolation forward model from 0-deg to 157.5-deg with an increment of 22.5-deg. A MATLAB program for 2D reconstruction is made based on Equation 2.5-2.8. The eight projections were imported into the made program with relaxation factor $\lambda = 0.55$ and iterated 10 iterations. Figure 2.15(c) shows the reconstructed image. The approximate density and general shape and locations of the ellipses are well reconstructed.

A second phantom of 48-by-48 pixel greyscale Purdue logo is made with photoshop, as shown in the left side of Figure 2.16. The color bar shows the 16-bit greyscale value of the images. The shape of the second phantom is slightly complex than the first phantom. The result of the simulated reconstruction is shown in the right side of Figure 2.16. Similar to the first phantom, the general shape and approximate greyscale values of the original image are captured by reconstructing 8 projections using ART method.

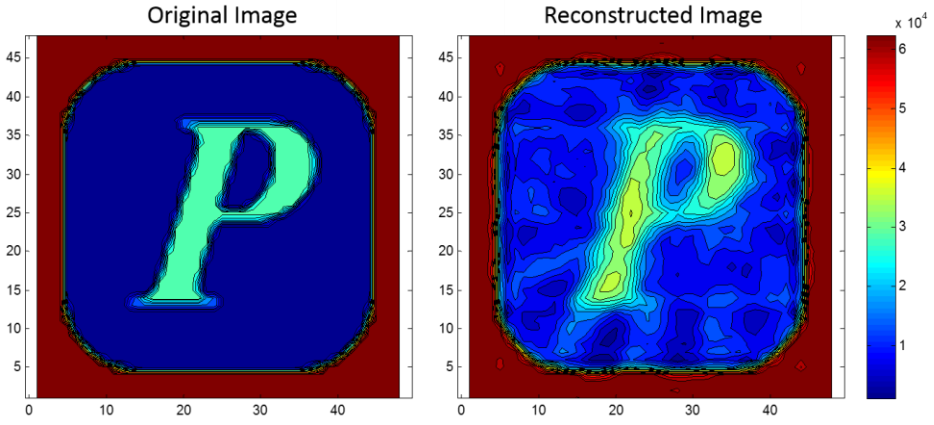

Figure 2.16 Simulated ART reconstruction of Purdue logo.

It is found that the major factor to influence the quality of the reconstruction is the number of projections: the second phantom of Purdue logo is reconstructed from 3 projections to 16 projections, where the letter “P” is clearly recognizable when the number of projections is 8-16, the letter is somewhat recognizable when the number of projections is 4-7, and the letter is not recognizable when the number of projections is only 3. It is noted that these two simulated reconstruction cases are based on the projections without noise. However, in the reconstruction of experimental data, the noise is inevitable. Moreover, the accuracy of the angle is also found important to the reconstruction. In next chapter, the signal-to-noise levels and alignment of the experimental setup are verified via physical phantoms.

CHAPTER 3. PRELIMINARY STUDIES

3.1 Static Phantoms

Before 3D reconstructing the specimens, three different imaging phantoms were manufactured to test and verify if the inputs are correct, the locations of X-ray sources, specimen and detectors are within the tolerance, and the 3D tomography reconstruction algorithm works. The name "phantom" is originally used in the medical field to evaluate the performance of X-ray imaging system by simulating living organs but avoid living subjects. The phantom in this research indicates a static object with known geometry and properties to verify the experimental setup.

A CAD view of the first phantom is shown in the upper left picture of Figure 3.1. Four steel pins of different shapes (full-length, half-length towards the bar, half-length towards the sample, and full-length with a gap in middle) were inserted into a nylon ring holder. The nylon can be treated nearly transparent under given conditions. The location of these four pins can be determined by tomography reconstruction. Two phantoms were used: one with four 0.8-mm-diameter (D-1/32") pins and one with four 0.4-mm-diameter (D-1/64") pins. The upper middle picture shows a typical 2D projection, where the top part shows the phantom with D-1/32" pins, and the bottom part shows the phantom with D-1/64" pins. It is noted that the projection shown here is inverted for the visual enhancement, where the white area indicates heavy-attenuated feature and the darker area indicates less attenuated region. An intensity threshold is applied to the images for better illustration, however, such threshold is not used in reconstruction process to avoid information lost. As mentioned earlier, tomoj plug-in of the ImageJ software is used for 3D reconstruction. The top and bottom pictures on right side show the reconstructed slice at Z=112 indicating the cross-section of the D-1/32" pins and the slice at Z=486 indicating the cross-section of the D-1/64" pins, respectively. The Z direction is shown in the CAD model and the projection, which is the pixel number in the Kolsky bar direction. It is found the location and the diameter of the pins can be clearly reconstructed. It is noted that the reconstructed slices show small number of artifacts induced by the algorithm, such as the two white dots on the left side of the Z=112 slice and the white dot near the right edge of the Z=486 slice. The total artifacts in this phantom reconstruction can be viewed along with the pins in 3D, as shown in bottom part of Figure 3.1. Such artifacts are probably due to heavy undersampling, since the number of projections is limited to four. In general,

iterative reconstruction algorithms significantly reduce the number of artifacts comparing to Radon-transformation-based algorithms, especially when the number of projections is limited [30, 31]. However, with only four projections, it is inevitable to avoid the artifacts with current reconstruction techniques. It is noted that the number of artifacts would reduce with larger number of projections. In this phantom, the smallest feature size can be clearly defined is 0.4 mm. It is noted that, for a very spares dataset case like the first phantom, the smallest feature can be even smaller if the signal-to noise ratio is sufficient.

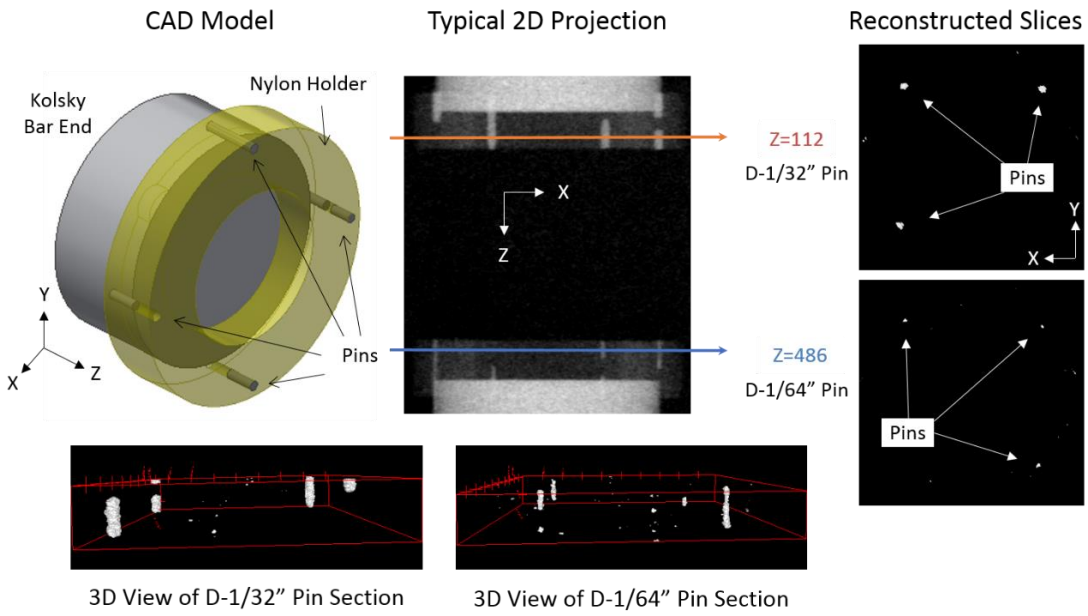

Figure 3.1 A first phantom verification of the setup and reconstruction algorithm via two types of pins with different diameters.

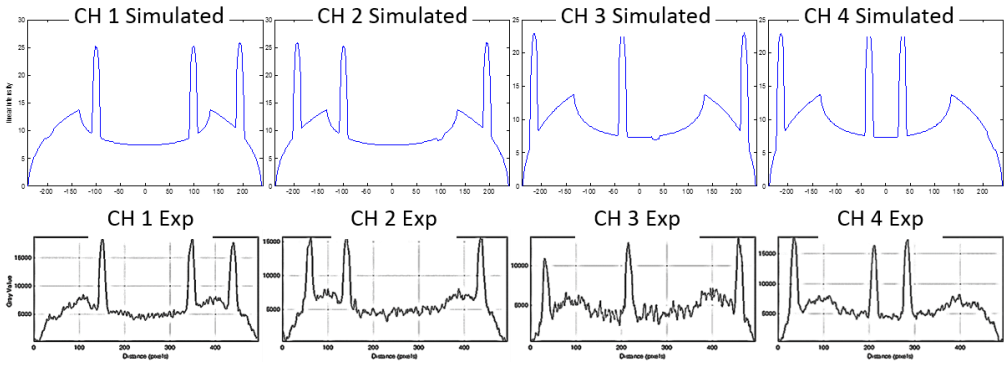

Figure 3.2 Intensity line-plots from experimental projections VS simulated projections for the pin-based phantom in Figure 3.1.

A simulated phantom was also modeled based the CAD dimensions and was simulating projected by Radon transform without noise. The simulated projections (shown in Figure 3.2 as the inverted intensity line-plot) match with experimental projections. The first phantom verified that the relative locations of the system is correct, and the ART algorithm successfully reconstructed the sparse dataset with very small number of artifacts, where the sparse dataset is given by few small pins relatively far away from each other.

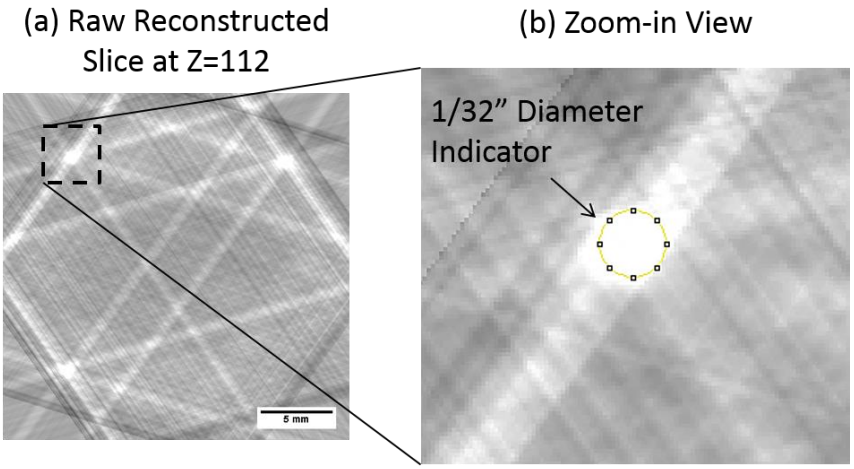

Figure 3.3 A raw reconstructed slice for the first phantom without visual enhancement: (a) reconstructed slice at Z=112, and (b) a zoom-in view of the 1/32” pin.

Figure 3.3 shows a raw reconstructed slice for the first phantom without any visual enhancement. Few lines can be found in the reconstructed slice. It is noted that those lines are artifacts from the reconstruction algorithm and can be mostly eliminated by using regularization-base algorithm, or a threshold over the image intensity as mentioned earlier. Figure 3.3(b) shows a zoom-in view of the 1/32” pin, where the CAD dimension is also indicated in the figure. It can be found the white area is very close to the CAD dimension.

Figure 3.4 shows the intensity plots for Figure 3.3(a). Figure 3.4(b) plots the intensity in the line as shown in Figure 3.4(a), where the two peaks indicate the pin location. It can be found that the distance between mid-points of two peaks is also very close to the CAD dimension. Figure 3.4(c) shows the surface plot for the intensity, where the high peaks indicates the white area in the reconstructed slice. Figure 3.4(d) shows the intensity surface plot after applying threshold. It can be found that most of the line artifacts is eliminated. However, it is noted that the threshold is not a subjective process since the value of threshold varies based on the phantom. In this research, the

threshold applying is an approximate process after the reconstruction. As mentioned earlier, the threshold is not used before the reconstruction to avoid losing information.

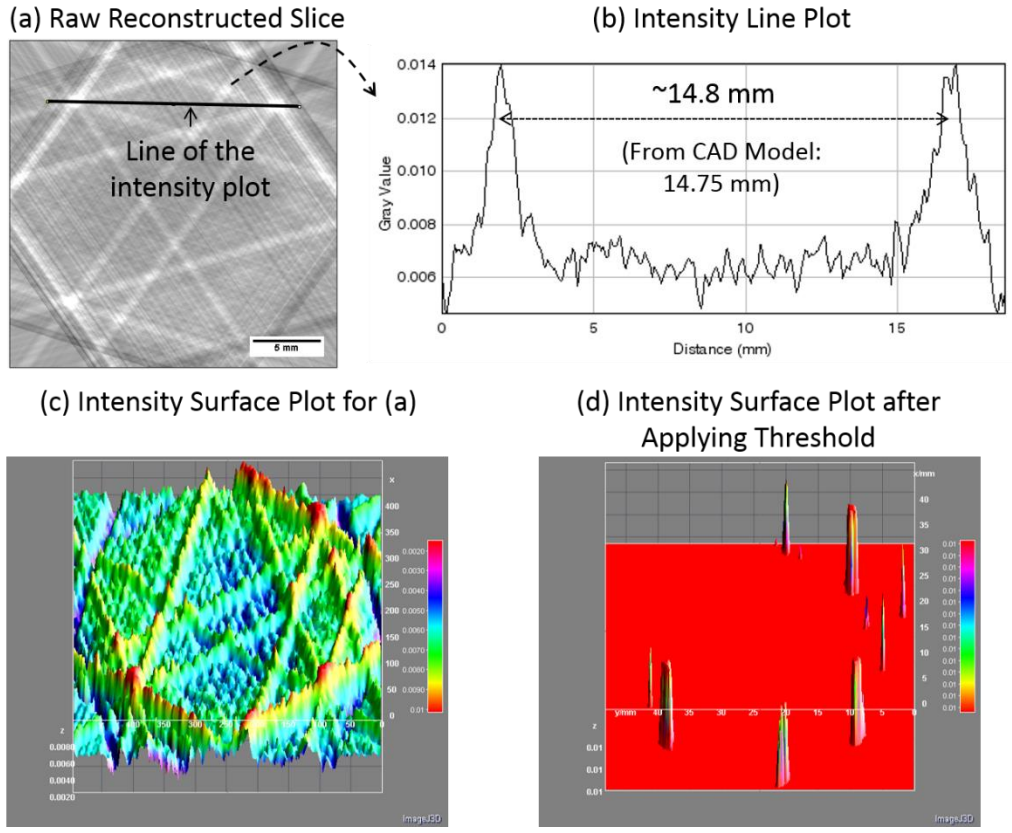

Figure 3.4 Intensity plots of the reconstructed slice from Figure 3.3: (a) raw reconstructed slice, (b) intensity line plot where the line is indicated on (a), (c) intensity surface plot without threshold, and (d) intensity surface plot with threshold.

In a second phantom (shown in Figure 3.5), an aluminum disk with four through holes was machined to examine the reconstruction ability to detect small voids in a bulk material (dense dataset). As discussed earlier, it is favorable for the reconstruction algorithm to reconstruct sparse datasets. The circular holes in a bulk material can serve as a general non-favorable scenario for the reconstruction process. It is noted that the log differences of attenuation of the holes in all directions are the same. Thus, the reconstruction might not improve or worsen when rotating the phantom. As shown in Figure 3.5(b), the diameters of four holes are 0.10” (2.54 mm), 0.08” (2.06 mm), 0.06” (1.52 mm), and 0.04” (1.09 mm), respectively. Figure 3.5(c) shows a typical 2D projection from the phantom, where the white area shows low attenuation and the darker area shows higher attenuation. One can find three vertical bands (Z direction) in lighter grey color of

the projection. However, due to inherent noise associated with the imaging system, it is very hard to distinguish the fourth one. Figure 3.5(d) shows the line plot of the log attenuation (equation 2.2-(b)) in the horizontal direction of Figure 3.5(c), where the dashed line is the line plot from a single line (Z=125), and the solid line is the line plot of the average of 200 lines. It is noted that a lower pixel value feature (with higher attenuation) has a lower absolute noise but a higher noise ratio. In the averaged curve, it can be seem that there exist four convex regions: 1) from ~100 to ~120 pixels, which is probably from the 0.04" hole, 2) from ~140 to ~190 pixels, which is probably from the 0.1" hole, 3) from ~220 to ~270 pixels, which is probably from the 0.06" hole, and 4) from ~290 to ~330 pixels, which is probably from the 0.08" hole. However, due to the noise, only the two larger regions from the 0.1" and 0.08" holes are visible in the Z=125 curve. In this case, before reconstruction, a median filter with radius = 1 pixel in horizontal direction (X and Y) and radius = 2 pixels in vertical direction (Z) is applied to reduce the noise. Figure 3.5(e) shows a typical reconstructed cross-sectional view, where the white area indicates high attenuation and the darker area indicates low attenuation. The D = 0.1" and 0.08" holes are visible without further visual enhancement. Figure 3.5(f) shows the color enhanced image of the Figure 3.5(e), where the D = 0.06" hole is slightly visible. The grayscale colorization method used here is a spectrum lookup table built-in from ImageJ software. It can be found that the number of artifacts is apparently increased comparing to the first phantom case. It is noted that a strong filter with strong regularization of the experimental projections would reduce the noise, and thus might improve the quality of the reconstructed image. However, stronger filter would also introduce higher bias to the projection and might blur the edges and eliminate small-sized features. Without further filtering or visual enhancement, the smallest feature can be clearly defined in a very dense dataset like the second phantom is 2 mm. Such result makes sense as both traditional radiography cannot well distinguish a crack if the thin-direction of the crack is imaged.

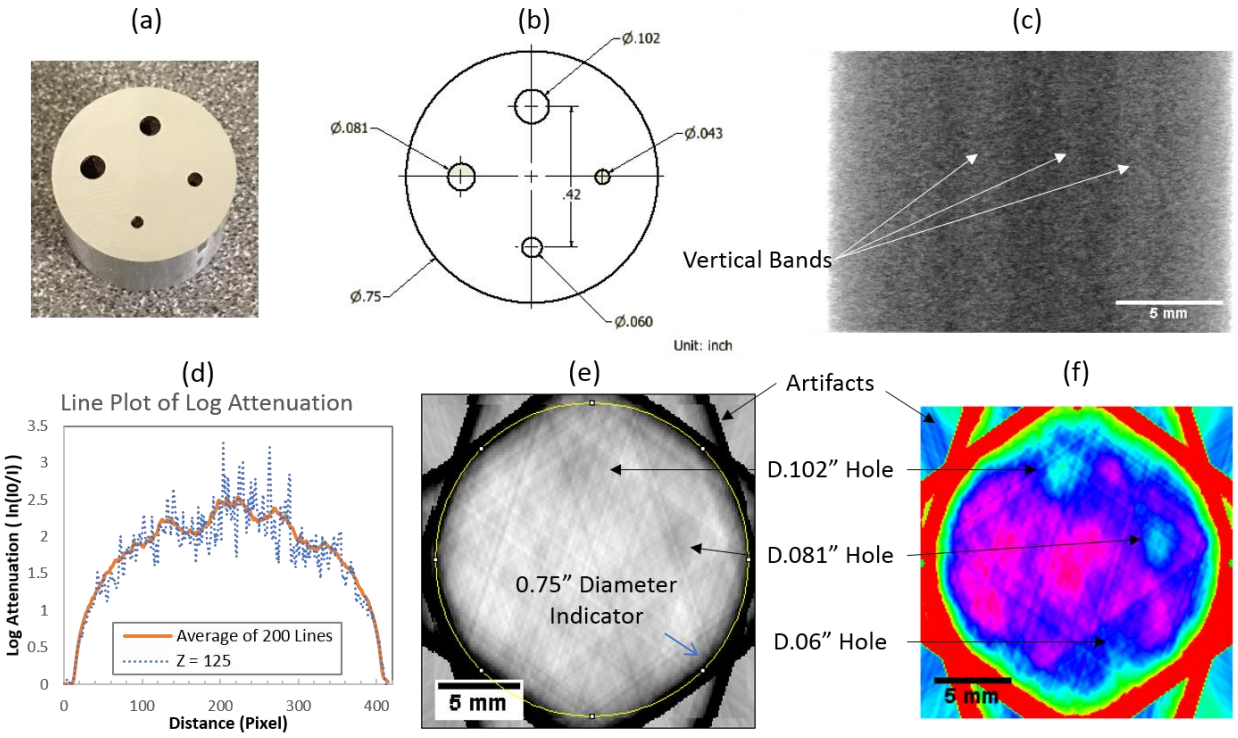

Figure 3.5 A second phantom verification via an aluminum disk with four through holes in different diameters: (a) a photo of the phantom, (b) dimensions of the disk and the through holes, (c) a typical 2D projection where the white area shows low attenuation and the darker area shows higher attenuation, (d) log attenuations along horizontal lines of the projection (c), (e) a typical reconstructed cross-section where the white area shows high attenuation and the darker area shows low attenuation, and (f) color enhancement of grayscale cross-sectional image (e) via spectrum lookup table.

A 3-D printed aluminum model serves as the third phantom to examine the reconstruction ability between very sparse (first phantom) and very dense (second phantom) dataset. As shown in Figure 3.6(a), the third phantom consists of a circular base, a ring on the top with four holes of different diameters, and four tapers connected between the base and the ring. The dimensions of the tapers and the ring are shown in Figure 3.6(b). Figure 3.6(c) shows a typical 2D projection, where one can easily find the shape of four tapers and the center hole of the ring. Figure 3.6(d) shows a reconstructed cross-sectional slice view from side direction, where two tapers can be clearly determined. The ring can also be distinguished. However, the reconstructed attenuation (or voxel grayscale value) of the center hole in the ring is higher than the empty space attenuation. This is probably due to the nature of the reconstruction algorithm with limited number of projections (like artifacts), and the non-linearity due to the large diameter of the aluminum ring. Figure 3.6(e) shows

a 3D volume view of the reconstructed phantom. Although there are still some artifacts, all tapers (including the smallest taper) can be visualized. The center hole from the top of the structure can be clearly visualized. However, only the largest hole (D = 0.10”) can be apparently defined in the reconstructed image, which indicates a non-favorable case similar to the second phantom. For the taper section of this third phantom, the smallest feature size can be clearly defined is 1 mm.

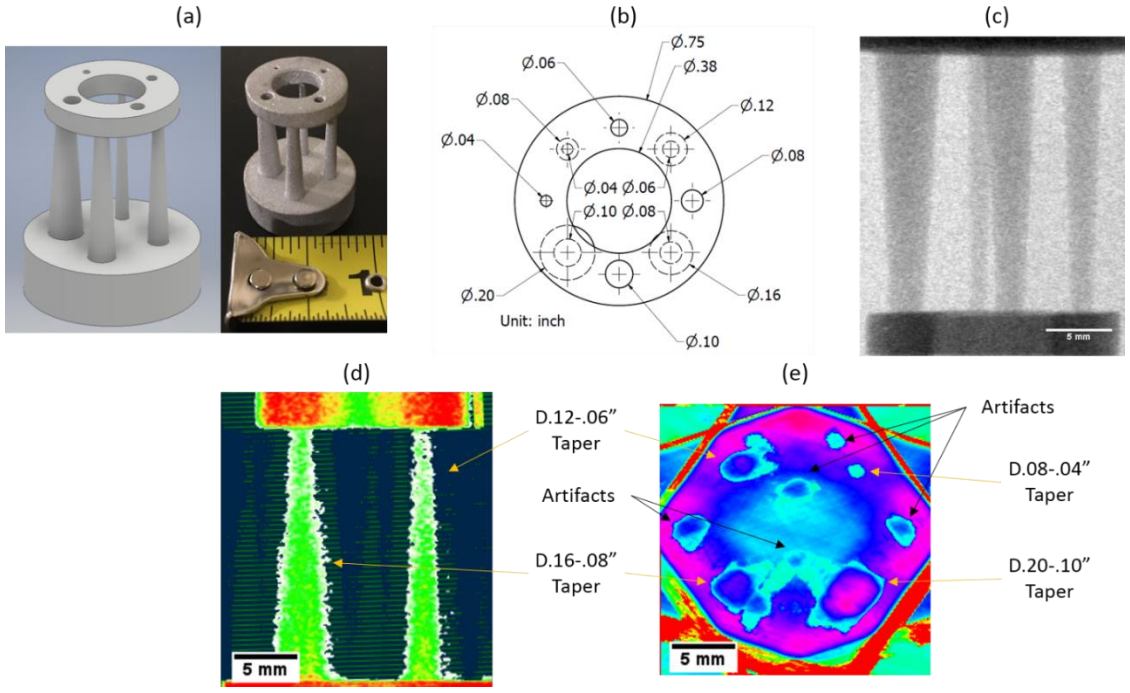

Figure 3.6 A third phantom verification via a 3D-printed aluminum model: (a) isometric view of CAD model and the photo of the phantom, (b) dimensions of the phantom, (c) a typical 2D projection where the white area shows low attenuation and the darker area shows higher attenuation, (d) a reconstructed cross-sectional slice view from side direction, where the view is enhanced by spectrum lookup table, and (e) a reconstructed 3D volume view from top-down direction, where the view is enhanced by spectrum lookup table.

It can be found that the reconstruction quality and the minimum recognizable feature is dependent on the noise level. Figure 3.7 summarized the intensity line plots from all three phantoms. From which one can find that the noise increases with respect to log attenuation. It is reasonable since a higher attenuation results in lower received X-ray intensity, which leads to higher noise ratio. The detail discussions on noise ratio with respect to received X-ray intensity is presented in Chapter 6. It is noted that the noise ratio is defined as the standard deviation of the signal divided by the average received X-ray signal. The observed noise ratios are ~9.6% and ~7.9% for the center

location of the disk phantom and the center location of the nylon holder of the pin-based phantom, respectively. The relative differences between the feature signals (i.e. the holes for the second phantom) and the surroundings are ~14%, ~11%, ~8.3%, and 5.9% for the 0.1", 0.08", 0.06" and 0.04" hole, respectively. Only the 0.1" and the 0.08" hole has the feature-signal-to-noise ratio larger than 1 (where they are identified in the reconstructed slice (Figure 3.5(e)) without visual enhancement). On the other hand, the relative difference between the pin and the surrounding nylon holder is ~77%, which is significantly larger than the noise (7.9%). It is reasonable that the reconstruction quality is better for the first phantom since the feature-signal-to-noise ratio is much higher than 1.

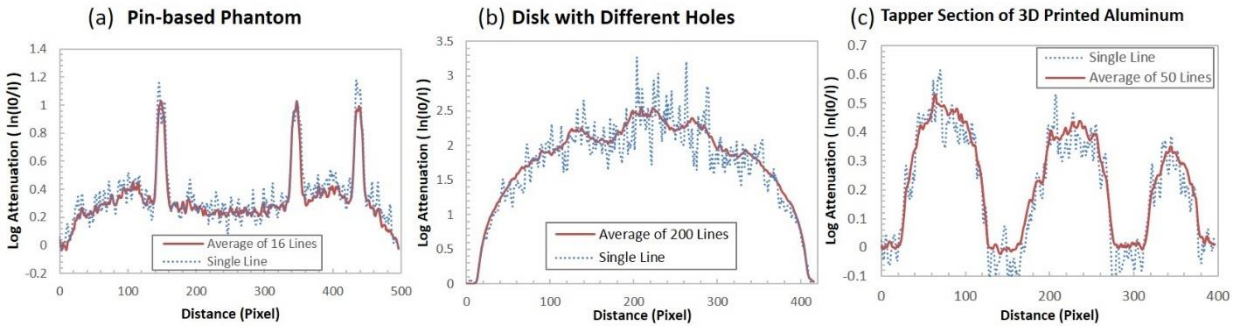

Figure 3.7 2D projection noise: line plots for (a) the first phantom with pins, (b) the second phantom of aluminum disk with holes, and (c) tapper section of the third phantom.

3.2 Uniaxial Compression of Chalk

Preliminary studies were conducted on dynamic loading of two materials to study the application range of the built flash X-ray system. Chalk is firstly selected for its brittleness and economy reason. Chalk is commonly made of Calcium carbonate with small amount of talcum or potato starch. It is mostly used for drawing on pavement or concrete sidewalks. Commercial grade chalks were bought and machined to cylindrical shape with 9.5 mm in diameter and 9 mm in length. Due the large impedance difference between the bars and the specimen, a rectangular incident loading pulse with a smoothed ramp rising edge was used to deform the specimen under a relatively constant strain rate. To deform the specimen to a large strain level, a 2.5 m long aluminum striker is used, which can generate a ~1 ms incident pulse. Figure 3.8(a) shows an averaged uniaxial compression stress-strain response from uniaxial compression of chalk at a constant strain rate of 450/s (averaged from 5 identical measurements). The error bars on the curve is the standard

deviation from interpolating the 5 stress-strain curves. From the averaged curve, the stress increases drastically to ~5.25 ± 0.71 MPa at ~0.7% strain, then drops to a relatively steady level of 2-3 MPa, and gradually decreases as the pieces cracking and flying out. Such gradual breakage is probably due the sticking component added to the commercial chalk. Four typical 2D projections were taken on four identical specimens with same loading conditions at 11%, 19%, 25%, and 43% strain, respectively. It is noted that the original images were in grey scale (like Figure 3.5(c) and Figure 3.6(c)). Artificial color mapping was used for better illustration. At 11% strain, the image shows a center crack parallel to loading direction, such center crack is probably induced by the tensile stress perpendicular to the loading direction near the internal defects; at 19% strain, the center crack expands, the lower end of the specimen becomes mushroom shaped and some debris ejects out from main body, where such mushroom shaped region is very close to the bar end indicating possible stress concentration at the bar-specimen interfaces; at 25% strain, the center crack shrinks slightly, and more debris flies out; and at 43% (near the end of loading), the specimen disintegrates. It is noted that the X-ray density of the chalk is very low, the average log attenuation (Equation 2.2-(b)) at center of the specimen is only ~0.35. Thus, the specimen does not have enough contrast to the background as shown in the 2D projections. Considering the inherent noise associated with the image and the artifacts induced by the reconstruction algorithm, the resulting 3D slices were hardly recognizable. For the specimens without enough attenuation like chalk, this method, however, can provide qualitative information to observe the 2D fracture behaviors from different angles.

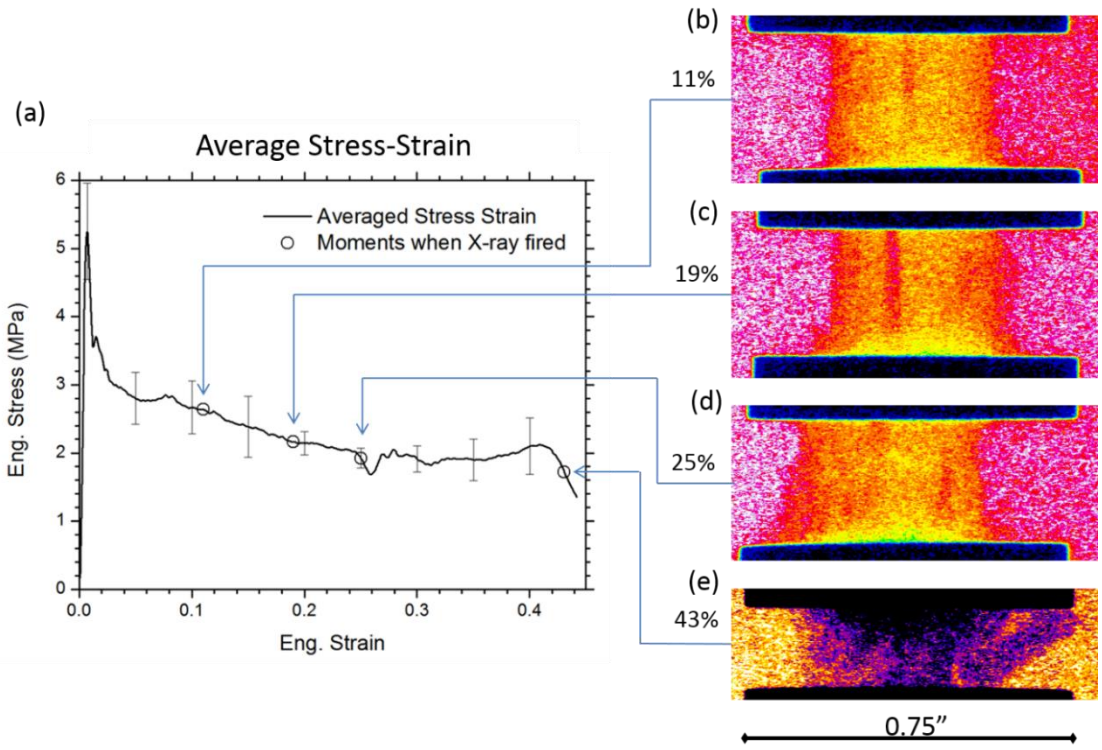

Figure 3.8 Uniaxial compression of chalks: (a) averaged stress-strain response, (b) a colorized 2D projection at 11% strain, (c) a colorized 2D projection at 19% strain, (d) a colorized 2D projection at 25% strain, and (e) a colorized 2D projection at 43% strain.

3.3 Uniaxial Compression of Limestone

To achieve a better 2D projection contrast, it is desired to increase the X-ray attenuation density. A second preliminary study was conducted for limestone specimens under uniaxial compression. Limestone is a form of sedimentary rock, which is widely used in civil construction applications such as building material and component of concrete. Frew *et al.* [33], Richard *et al.* [34], and Petrov *et al.* [35] conducted dynamic uniaxial compression experiments of different kind of limestones using Kolsky bar from 70/s to 570/s and found a large scatter in terms of dynamic compressive strength, depends on where the limestone is harvested and the equipment and testing condition of the Kolsky bar experiments. The reported compressive strength around 100/s is range from 11 – 120 MPa, and the reported critical strain at peak stress is range from 0.6% - 2.3%.

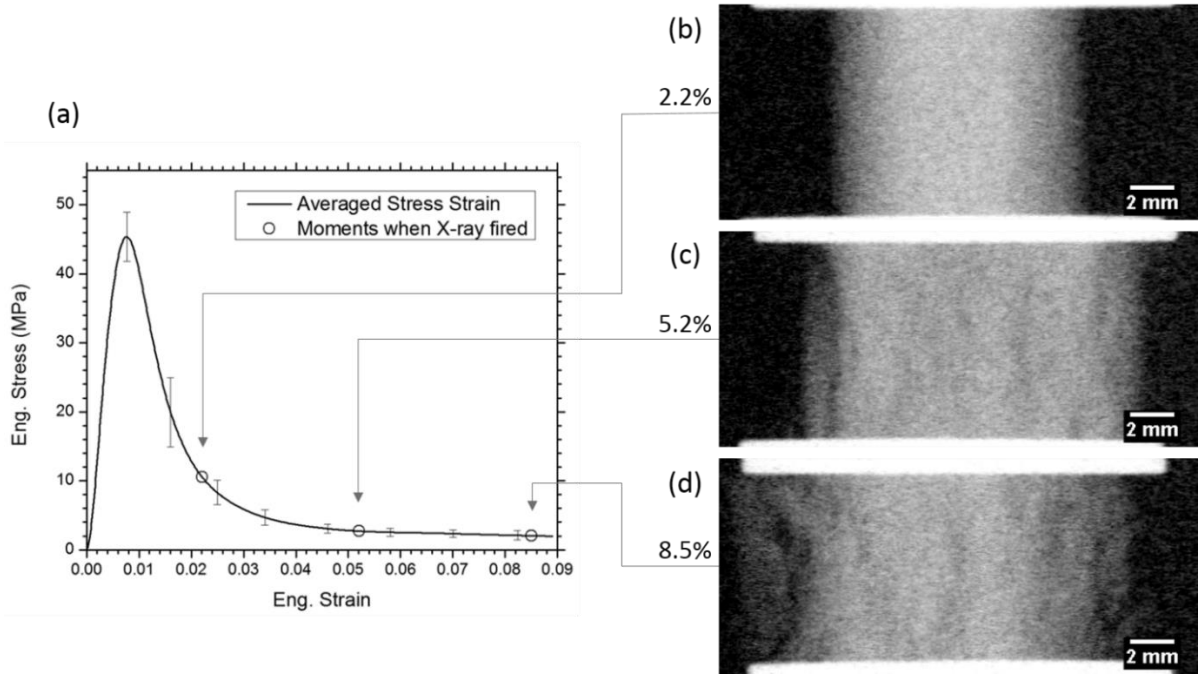

Figure 3.9 Uniaxial compression of limestones: (a) averaged stress-strain response, (b) an inverted 2D projection at 2.2% strain, (c) an inverted 2D projection at 5.2% strain, and (d) an inverted 2D projection at 8.5% strain.

In this study, commercial grade limestone blocks were bought and sliced into small cubes with width ≈ height ≈ length ≈ 9.5 mm. A pulse-shaper-generated bi-linear ramp incident pulse is used to deform the limestone specimen at a nearly constant strain rate about 80/s. The averaged stress strain curve is shown in Figure 3.9(a). Such a curve is averaged from 6 identical measurements. The peak stress of limestone is 45.4 ± 3.6 MPa at ~0.77% strain. Unlike chalk, the stress drops to nearly zero after the initial breakage. Three typical 2D projections were acquired from three identical specimens loaded under identical rate, as shown in Figure 3.9(b)-(d). The trigger delay time are 305 μs, 390 μs, and 490 μs for the corresponding engineering strain of 2.2%, 5.2% and 8.5% when X-ray fired, respectively. At 2.2% strain, the cracking inside the specimen is not apparently visible as shown in Figure 3.9(b). At 5.2% strain, Figure 3.9(c) shows multiple cracks parallel to the loading direction running inside the specimen, which indicates the specimen is failed due to axial splitting where the tensile stress perpendicular to loading direction tears the specimen apart. Unlike chalk which only shows a major center cracks, limestone breaks due to many cracks. At 8.5% strain, Figure 3.9(d) shows even more cracks as compared with the projection at 5.2%

strain. It is noted that due to the cube-shape of the specimen, material at the corner of the specimen might have stronger stress concentration.

The contrast of limestone with respect to background is much better than that of chalk. The average log attenuation at center of the specimen is around 1.2. However, due the fact that the limestone breaks into many pieces, the artifacts in 3D reconstruction covered the real features. In the trial reconstructed slices, many possible lines can be visualized. However, it is very difficult to determine if the lines shown in the reconstructed slice is a representation of a crack or the artifacts. The features inside the specimen are not visible. Thus, it is favorable for the reconstruction process if the target specimen breaks into limited pieces.

3.4 Plate-ball Compression of Aventurine Spheres

Plate-ball compression experiments were conducted on aventurine spheres. Aventurine is a form of natural quartz with a density of 2.64-2.69 g/mm^3. In this study, spheres with a diameter of 20 mm were used. To prevent the damage of bar ends, thin hardened A-2 tool steel plates were placed between the specimen and the bar ends. A thin heat shrink tube was used to hold the sphere from dropping. It is noted that the heat shrink tube is soft and can be easily deformed by hand. Considering the axial force to break the sphere is in the order of few kN, the heat shrink tube would not confine the specimen to alter its stress state. The X-ray was fired twice for each measurement: one before the deformation and one during the deformation. The 2D results are shown in Figure 3.10. From force-displacement curves, the peak force is ~12 kN at ~ 0.37 mm. The initial low force region is likely due to the large diameter of the specimen and the non-linear contact between the sphere and the plate. The images shown in Figure 3.10(b) and (d) are the input by Equation 2.2(a). It is noted that the images are enhanced by fire lookup table, where the yellow region indicates the crack and the blue region indicates the specimen expansion.

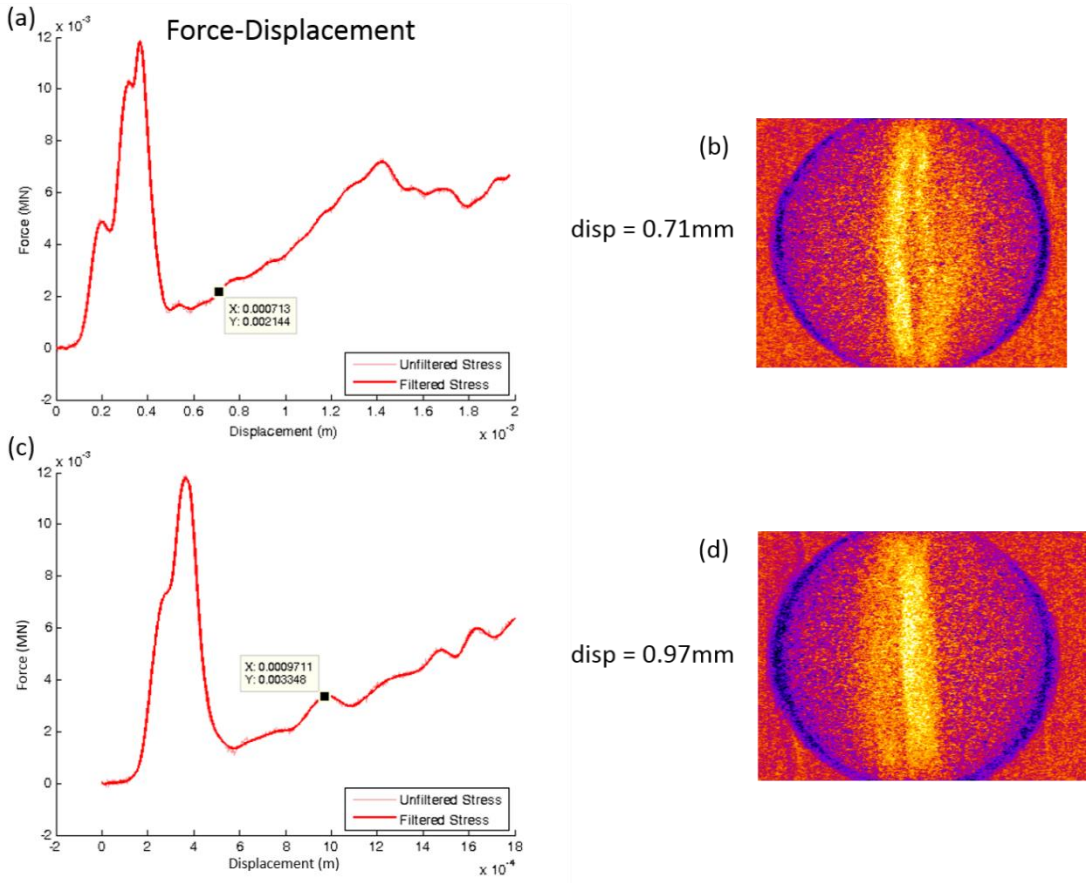

Figure 3.10 Plate-ball compression of aventurine spheres: (a) force-displacement of a first specimen, (b) a colorized 2D projection of the first specimen at 0.71mm displacement, (c) force-displacement of a second specimen, and (d) a colorized 2D projection of the second specimen at 0.97mm displacement.

Since for aventurine sphere compression, both un-deformed state and deformed state were imaged, a first attempt was conducted by reconstructing both states individually. A reconstructed slice from deformed state (Equation 2.2(b)) is shown in Figure 3.11(b), which shows one apparent crack around 70-deg from horizontal axis and one possible crack around 145-deg. The specimen is the same specimen shown in Figure 3.10(a)-(b). The reconstruction from same location using both states (Equation 2.2(a)) is shown in Figure 3.11(c), from which one can distinguish two cracks. Figure 3.11(d) shows a 3D view of the reconstructed object from Equation 2.2(a), where the threshold is applied to remove majority of the reconstruction artifacts. The crack width of the crack about 77-deg is measured to be ~0.7 mm, which is better than the worst-case scenario given by the second and third phantom. This is probably due to the crack direction is align to one of the X-ray

beam direction. It was observed that the crack around 150-deg has a larger width and higher noise than the other crack, which is probably due to it not aligned well with any of the X-ray beam. The angles between the two cracks from ART reconstruction, and from recovered specimen photo are 73.5±11 deg, 75±3 deg, respectively. The angle from ART reconstruction method matches with recovered specimen, which is shown in Figure 3.11(e). Both cracks are nearly parallel to the loading direction, which indicates the tensile stress is the governing stress for the two cracks to open and break the specimen into four. This finding matches the report by Parab *et al.* [39]. In this preliminary study, the tomography for the crack is successfully reconstructed as a result of (1) the specimen has appropriate log attenuation (maximum ~1.5 for the specimen used), and (2) the number of major cracks inside the specimen is only two. It is also noted that in the situation of this preliminary study, the reconstruction taking the difference of deformed specimen to un-deformed specimen is apparently improved from the reconstruction only taking the deformed specimen projections.

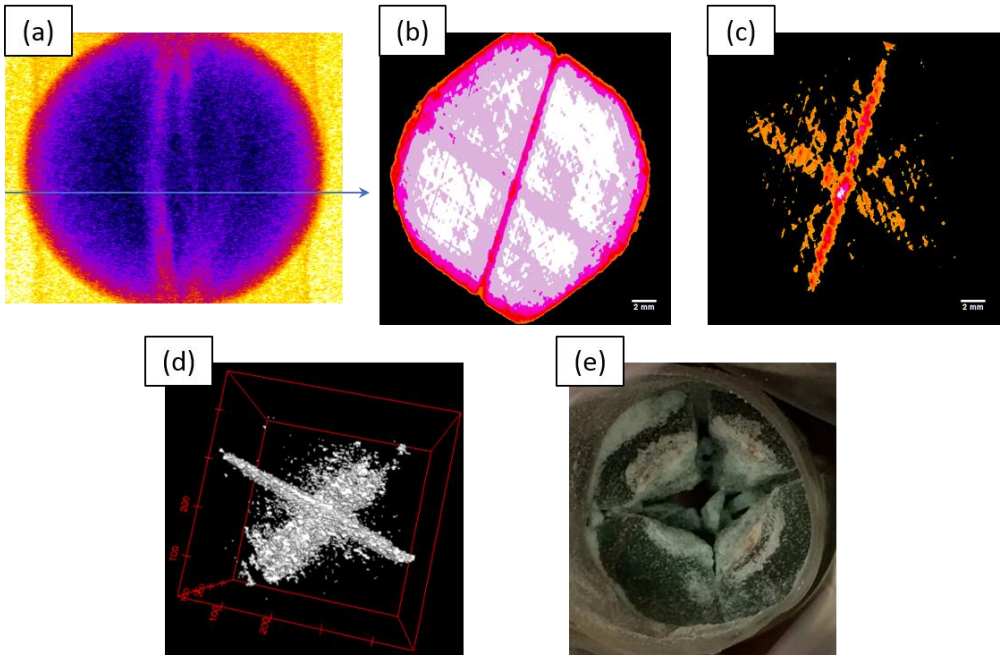

Figure 3.11 Tomography reconstruction of an aventurine sphere from Figure 3.7(a)-(b): (a) indication of the slice location in terms of a 2D deformed projection, (b) a colorized reconstructed slice from only deformed projections at Z=266 pixel, (c) a colorized reconstructed slice from both undeformed and deformed projections at Z=266, (d) a 3D view of the reconstructed object of (c), and (e) the recovered specimen after loading.

3.5 Summary

In this section, preliminary studies were conducted to verify the method and test the application range. Three static phantoms were manufactured for sparse dataset (the first pin-based phantom), dense dataset (the second aluminum disk phantom with holes), and a dataset in between (the third 3D-printed aluminum phantom). The result verified the inputs are correct and the relative locations of X-ray sources, specimen and detectors are within the tolerance. The reconstruction images show the worst-case clearly recognizable object size is 0.4 mm for the first phantom, 2 mm for the second phantom, and 1 mm for the third phantom, respectively. Uniaxial compression on chalk and limestone and plate-ball compression on aventurine sphere were conducted. The tomography reconstruction of the first two is not successful as the log attenuation of chalk is low resulting high noise and the number of cracks inside the limestone is too many resulting numerous artifacts in the reconstruction. The in-situ aventurine sphere under dynamic plate-ball compression is successfully reconstructed, given appropriate log attenuation and number of cracks. It is found that the smallest size of the crack aligning with one of the X-ray beam direction is better than the static phantom. Moreover, the reconstruction with both deformed specimen and un-deformed specimen is apparently better than the reconstruction only taking the deformed specimen in some scenarios.

CHAPTER 4. INDENTATION ON MACHINABLE CERAMICS

4.1 Machinable Ceramics

In this section, dynamic indentation experiments were conducted via indenting a spheroconical tip into cylindrical specimens to investigate the breakage phenomena of two types of machinable ceramics. Machinable ceramics are glass-bonded mica ceramic materials. Based on different brands, the types of mica filler and the percentage of glass-mica ratios are different. Machinable ceramics are widely used in thermal and electrical insulation applications such as high voltage electronic components and thermal barrier coatings, due to their low thermal conductivity, high dielectric strength, flame retardancy, geometric stability, and relative high machinability (can be machined by conventional metal working tools) comparing to traditional ceramics. In this study Mykroy/Mycalex ® 550 (short for M/M) developed by Crystex Composites [36] and Macor ® from Corning [37] were used. Table 4.1 lists a comparison between MM and Macor. The dimensions for M/M specimens are 9.5 mm in diameter and 14.5mm in length, and for Macor specimens are 9.6 mm in diameter and 9.8 mm in length.

Table 4.1 Basic Properties of Two Types of Machinable Ceramics [36, 37].

	M/M 550	Macor
Density (g/cm^3)	2.7	2.52
Color	Light Gray	White
Thermal Conductivity (W/m.K)	1.15	1.46
Quasi-static Compressive Strength (MPa)	276	345
Young's Modulus (GPa)	82.7	66.9

4.2 Experimental Setup and Force Displacement Response

A spheroconical indenter was glued to the transmission bar end for dynamic indentation. The schematic diagram is shown in Figure 4.1. The angle of the cone is 90-deg. The indenter is made of hardened A-2 tool steel: an A-2 steel rod in annealed state was purchased and machined to shape, the machined part was then heated to 940 ^{o}C and quench in dry air blast, the quenched part was

tempered at 230 ºC for 2 hours. The hardness of tempered part can reach 59 HRC. To prevent the indenter indents into the bar, single loading stopper was used to stop the movement of incident bar after one loading pulse.

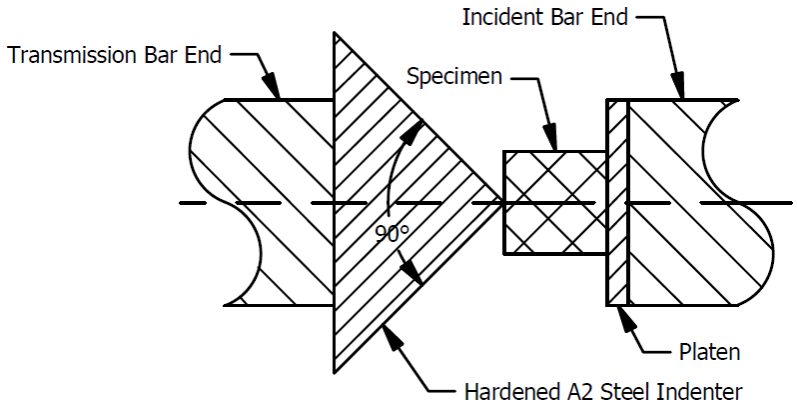

Figure 4.1 Schematic of spheroconical indentation setup.

A trapezoidal incident loading pulse with a flat top was used to deform the specimen under a relatively constant deformation velocity. The average deformation velocity for both materials are 2.1 m/s. The averaged force-displacement curves and corresponding error bands for both materials are shown in Figure 4.2. The error bands shown in the figure is the standard deviation from averaging multiple curves. It can be found that the initial rising region of both materials are similar (indentation depth less than 0.15 mm), which is probably due to the Young's modulus of MM is higher than that of Macor, and the length of MM specimen is also higher than that of Macor. However, in traditional indentation experiments, specimen thickness is not an apparent function of indentation response, especially for the ratio of contact radius to specimen thickness << 1 [53]. It is noted that under contact theory, the force is proportional to the square of the indentation depth curve for a rigid spheroconical tip into an elastic half-space [38]. However, the initial rising region is not in a quadratic shape. This region can be mathematically fitted into $y = ax^n$, where n ≈ 1.25 instead of 2. Such discrepancy might be due to the fact the machinable ceramic is technically a bulk of bonded small glass-mica particles. The response under micro-structure level is not linear-elastic, but a combined mechanism of deformation of individual particles and re-arrangement/breakage of groups of particles. What's more, the compliance of the indenter and gluing layer need to be considered, which might result in the real indentation depth to be smaller

than the displacement detected by bar strain gages, especially at sub-0.1 mm level. The force from MM specimen deviates from initial rising region at ~ 0.15 mm and the force from Macor deviates at ~0.25 mm, which is an indication that part of the specimens permanently deformed or partial failure. The peak forces and the displacements at peak force for each material are listed in Table 4.2. The MM specimen has a relatively long after-breakage region (from displacement ~0.3 mm to ~0.8 mm), which indicates a gradual failure; while the force of Macor specimen sharply drops to zero after breakage, which indicates a sudden failure. It is noted that the force of Macor specimen oscillates to below zero due to the sudden failure of the specimen and the inertia of the steel indenter.

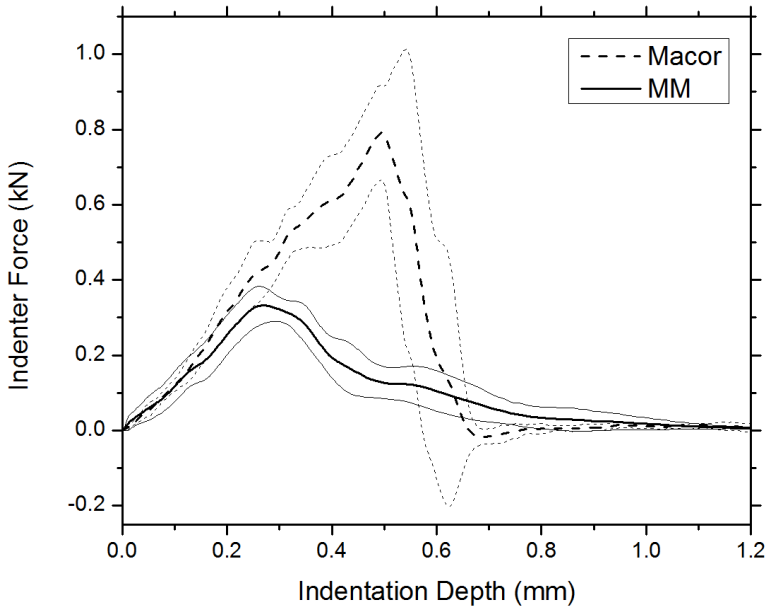

Figure 4.2 Averaged force displacement from spheroconical indentation of Macor and Mykroy/Mycalex 550.

Table 4.2 Peak Forces and Critical Displacements of Two Types of Machinable Ceramics.

	M/M 550	Macor
Peak Force (N)	353±26	984±73
Critical Displacement (mm)	0.28±0.04	0.55±0.05

4.3 2D Projections

Figure 4.3 shows a typical set of 2D projections from an MM specimen, where the displacement when X-ray fired is 0.39 mm. The images shown here are inverted where the whiter area indicates higher attenuation. Figure 4.3(e) shows the corresponding force displacement of the specimen, where one can find that the X-ray firing point is right after the force drop from the peak point. From the projections, one can find only Figure 4.3(c) shows a crack starting from the indenter point. The propagation direction of the crack is parallel to the loading direction, which indicates local tensile stress is the driving factor for the crack to open. It can also be found that the crack has not reach the other end of the specimen yet, which is reasonable since the force for this specimen has not reach zero yet when X-ray was fired. It is noted that due to the fact that the crack is very thin, if the crack direction does not align with the X-ray direction, such a crack cannot be visualized.

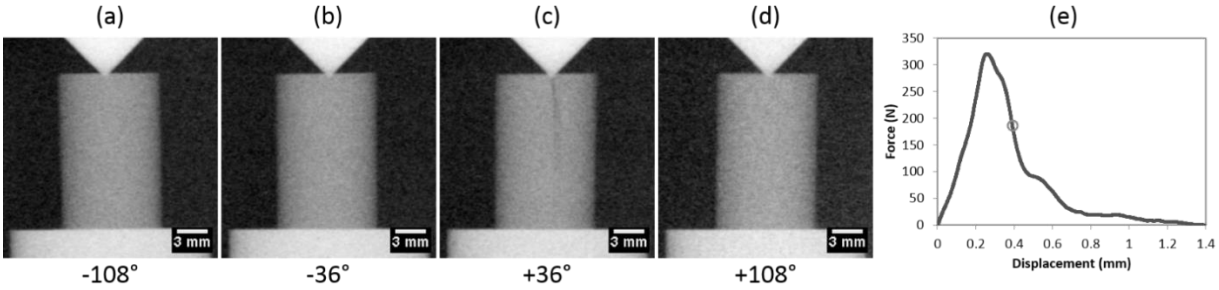

Figure 4.3 2D projections of a M/M specimen under dynamic indentation: (a) to (d) inverted 2D projections from different angles of the same specimen at the same time, and (e) specimen force displacement and the corresponding X-ray fire location.

Figure 4.4 shows a typical set of 2D projections from a Macor specimen, where the X-ray firing displacement is 0.68 mm, which is also right after the force drop from peak. From the projections, one can find three cracks, each from one projection (Figure 4.4(b)-(d)), and a possible crack in Figure 4.4(a). Unlike M/M, none of crack propagation directions is strictly parallel to the loading direction, indicates the crack opening stress is driven by both tension and shear for Macor. In the meantime, the crack shown in Figure 4.4(d) reaches the other end of the specimen, which is reasonable as the specimen force already drops to zero. However, by only few 2D projections, it is very difficult to determine how many total cracks running inside the specimen, since one crack in one projection might also appear on another projection.

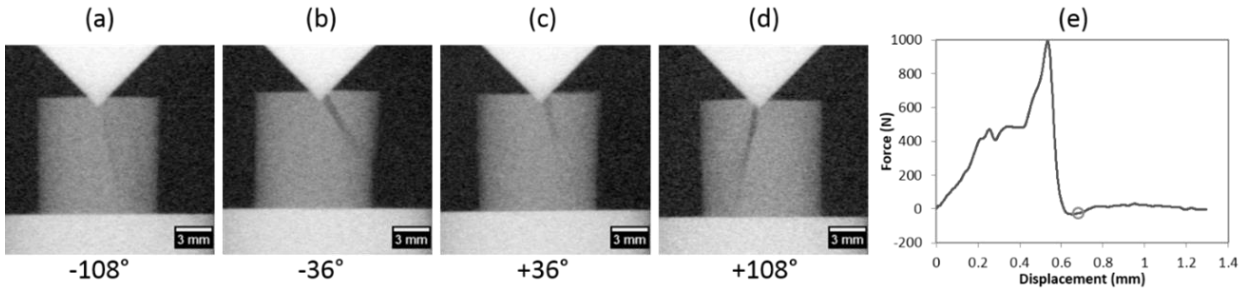

Figure 4.4 2D projections of a Macor specimen under dynamic indentation: (a) to (d) inverted 2D projections from different angles of the same specimen at the same time, and (e) specimen force displacement and the corresponding X-ray fire location.

4.4 Tomography Reconstructed Slices

The maximum log attenuation of M/M specimen and Macor specimen is ~1.1 and ~1, respectively. When the crack aligns with any of the projection direction, such attenuations are appropriate to give sufficient signal-to-noise ratio as mentioned in chapter 3. Figure 4.5 shows the reconstructed cross-sectional view for M/M specimen. The shown reconstructed slice located at Z = 100 which is 1.2 mm down from the indenter tip (shown in Figure 4.5(a)). As mentioned in chapter 3, the Z direction is the reverse loading direction of Kolsky bars (smaller Z indicates closer to transmission bar). The 2D projection in Figure 4.5(a) is the same projection in Figure 4.3(c). Figure 4.5(b) shows the reconstructed slice at the corresponding location, where one can detect an oblique crack. The width of the crack is about 0.35 mm. It is noted that in this chapter, only the deformed projections are used for reconstruction input. Figure 4.5(c) shows a color enhancement of the reconstructed slice by 16-color lookup table method, which is built in ImageJ software. Figure 4.5(d) shows another image enhancement via edge detection. As mentioned earlier there exist a considerable number of artifacts in the dense dataset. By performing the edge detection, most of the artifacts are illustrated as a single line. The double line, however, indicates an apparent crack since the corresponding parts are separated and there would be two edges presented. The above reconstruction result matches with the recovered specimen, where two major pieces were found, and their separation surface is parallel to the loading direction.

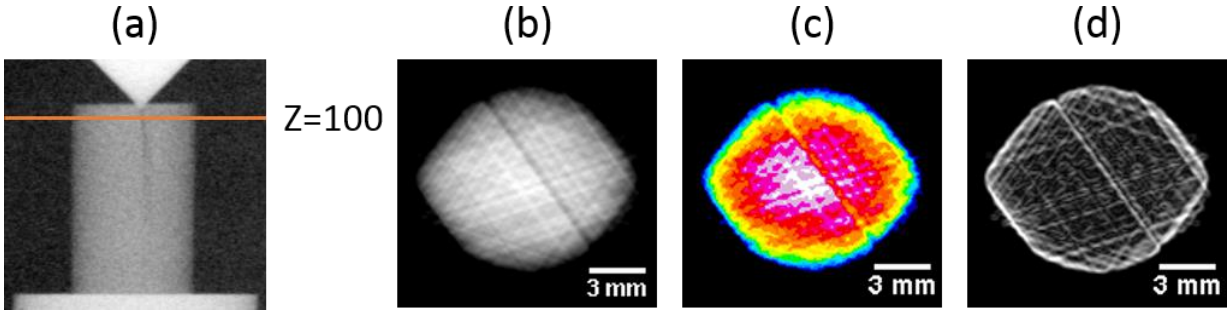

Figure 4.5 Reconstructed cross-sectional slice of a M/M specimen under dynamic indentation: (a) indication of the slice location in terms of a 2D projection, (b) reconstructed cross-sectional slice at Z=100 shown in greyscale, (c) color enhancement of (b) via 16-color lookup table, and (d) edge detection of (b).

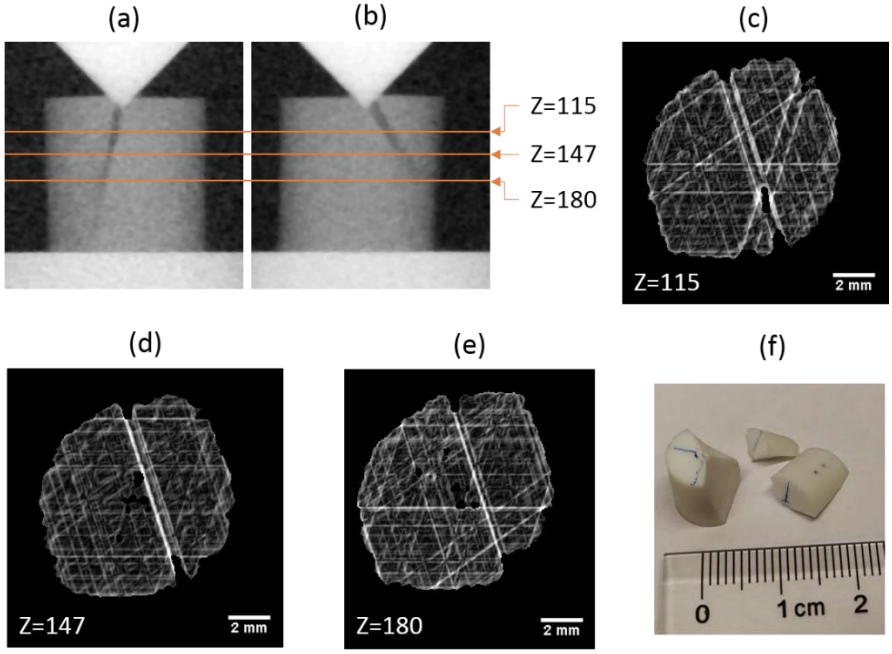

Figure 4.6 Reconstructed cross-sectional slices of a Macor specimen under dynamic indentation: (a)-(b) indication of the slices location in terms of 2D projections, (c)-(e) the edge of reconstructed cross-sectional slices at Z=115, 147 and 180, (f) photo of the recovered specimen after loading.

Figure 4.6 shows the reconstructed cross-sectional view for Macor specimen. Three slices are shown in Figure 4.6(c)-(e) where Z = 115, 147, and 180. The distances from the shown slices to the indenter tip are 1.41 mm, 2.96 mm, and 4.56 mm, respectively. In Z = 115 slice, one can find two oblique cracks, where the crack angles are 107° and 71°, and the crack opening widths are

~0.5 mm and ~0.6 mm, respectively. In Z = 147 slice, one can only find one crack. Such crack is the same crack of 107° in Z = 115 slice, while the width of the crack shrinks to ~0.4 mm. In Z = 180 slice, the width of the crack further reduces to ~0.3 mm. The above reconstruction result matches with the recovered specimen, which is shown in Figure 4.6(f), where one can find three major pieces.

4.5 Discussions and Future Works

In this research, it is noted that it is very repeatable for the M/M specimen to separate into two and the Macor specimen to break into three pieces. To further investigate the reason of such phenomena, microstructure images were taken for both materials. Figure 4.7 shows the cross-sectional images of both materials under 20X optical microscope, where the Macor (on the left) shows a nearly random particle orientation, and the M/M (on the right) shows that the majority of the particles orients in one direction (about -15° to horizontal direction). The randomized distribution of Macor matches with the SEM image from manufacture data sheet [37]. It is noted that the thin lines the in M/M image about 100° to horizontal direction is induced by cross-section cutting, rather than the feature by the material itself. On the other hand, the particle size in Macor is apparently smaller than the size in M/M. It is highly likely that under indentation the crack inside the specimen propagates along the particle direction. Since there is only one major particle direction in the specimen, it is reasonable for the M/M specimen to break into two clean parts as shown in Figure 4.5.

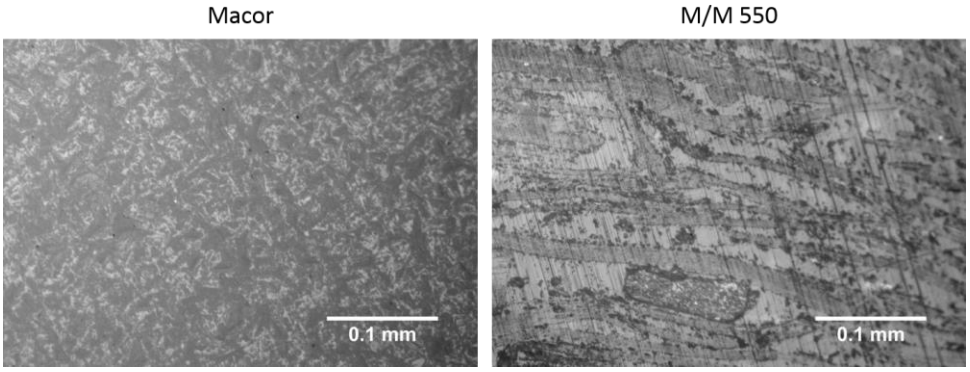

Figure 4.7 Cross-sectional photos of Macor and M/M 550 under optical microscope.

It is expected under spheroconical indentation the M/M failures along the particle direction. However, it is still unknown that whether M/M will crack along the particle direction again under

directional indentations (such as Vickers indentation). For dynamic Vickers indentation, researchers have observed that the brittle specimens crack along the diagonal directions of the square-based pyramid tip [52]. It would be interesting to investigate the crack directions of directional materials such as M/M under directional indentations, especially when these two directions are at an angle.

It is note that the specimen length for M/M used in this research is longer than the length for Macor specimen. Although traditional indentation experiments assume the specimen thickness has minor effect on the response when the ratio of contact radius to specimen thickness is small [53], a different specimen geometry might result in the difference in the post failure behavior. In this study, the M/M was observed a gradual failure behavior while the Macor was observed a sudden force drop after the peak force. It is possible that the crack takes a considerable amount of time to penetrant the M/M specimen. In future studies, the specimen length effect is proposed to observe the post failure during the dynamic indentation experiments.

Due to limited number of cracks, the flash X-ray tomography is a promising technique to visualize the post failure behaviors in-situ of dynamic indentation of brittle specimens. Currently, majority of indentation experiments visualize specimen performance after the indenter is removed, which the dynamic indentation cannot be imaged in-situ. Some use optical high-speed camera or synchrotron radiation with high-speed scintillator to visualize transparent specimens or non-transparent specimens, respectively. However, both techniques are limited by the crack direction (perpendicular to imaging axis for optical and parallel to X-ray beam for synchrotron radiation). The flash X-ray tomography expand the application range where the crack direction can be. As long as the crack direction approximately aligns with one of the X-ray beams, it can be well captured. It is noted that the larger number of projection angles can further increase the change to capture all the cracks and improve the reconstruction image quality.

4.6 Summary

In this section, spheroconical indentation experiments were conducted for two types of machinable ceramics to investigate the mechanical responses and failure mechanisms. The Macor shows a higher peak force and sudden force drop after failure, while the M/M shows a lower peak force with gradual failure behavior. In-situ X-ray projections and tomography reconstructions were taken for both materials right after the peak force. The images show that the Macor specimen

breaks due to two major cracks - one nearly parallel to the loading direction and another one oblique to the loading, while the M/M specimen breaks due to one major crack parallel to the loading. Microstructure images show that the Macor particle is randomized distributed, but the M/M particle is highly directional, which matches the in-situ breakage phenomena observed by X-ray.

CHAPTER 5. UNIAXIAL COMPRESSION ON 3D PRINTED SANDSTONE

5.1 Material

Recently, the rapid advancement of additive manufacturing industry (two other names are rapid prototype and 3D printing) has resulted the availability to directly print a 3D model commercially for a wide range of applications. The materials available for 3D printing includes thermo-plastics [40], metals [41], ceramics [42], and sandstones [43, 44]. The resolution (or layer thickness) of most commercial 3D printers can reach 0.05mm. 3D printing techniques enable to manufacture complex parts and assemblies which are not able to machine or costly to machine via traditional methods. However, the mechanical properties and the failure mechanisms for most of 3D printed materials have not been studied, especially for the response under dynamic loadings. Failure of a material is likely to start from the internal defects inside the material from manufacturing process. Such defects are generally not visible from the surface. X-ray tomography, however, is an appropriate tool to visualize them.

In this section, dynamic uniaxial compression on a 3D printed sandstone is conducted. The sandstone is commercially printed using ProJet 660 Pro 3D printers via two different on-demand printing service vendors [45, 46]. For both vendors, the material and the 3D printers are the same. The base printing material is VisiJet PXL Core powder (by 3D Systems) which consists 80-90% calcium sulfate hemihydrate. The powder is bonded together with a liquid inkjet binder (VisiJet PXL Clear by 3D Systems) to form a 3D model. The liquid binder is an aqueous solution with 0-1% 2-pyrrolidone. The model is post-treated with a fast-acting adhesive infiltrant coating to increase strength. The infiltrant used in this research is ColorBond/zbond® 90, which consists 80-100% 2-Methoxyethyl-2-cyanoacrylate. It is noted that the strength of printed specimen is greatly dependent on the type of infiltrant coating. The basic properties of this 3D printed sandstone from manufacture site is listed in Table 5.1. Three types of specimens were printed and coated with ColorBond: (1) cylindrical specimens with 10 mm in diameter and 10 mm in length, (2) ring shape specimens with 10-mm-ID, 14.2-mm-OD and 10-mm-L, and (3) dumbbell-shaped specimens with 25.5 mm total length, 10 mm length in gauge section and 6.3 mm diameter in gauge section. The cylindrical specimens were printed via both vendors [45, 46], while the ring shape and dumbbell-shaped specimens were printed via the second vendor [46].

Table 5.1 Basic Properties of 3D Printed Sandstone [46].

Quasi-static tensile Strength (MPa)		14.2	
Quasi-static tensile elongation (%)		0.23	
Composition	Base powder	Binder	Infiltrant
	VisiJet PXL Core	VisiJet PXL Clear	ColorBond
Density (g/cm^3)	2.6-2.7	1.0	1.04

5.2 Experimental Conditions and Mechanical Responses

A pulse-shaper-generated bi-linear ramp incident pulse is used to deform the 3D printed sandstone specimen at a nearly constant strain rate about 100/s. The striker used to load the sandstone has a length of 1.2 m. A typical set of incident, reflected, and transmitted wave is show in Figure 5.1(a). A typical set of strain rate and strain histories is shown in Figure 5.1(b), where the plateau region from ~0.4 ms to ~0.6 ms indicates that the specimen is under a constant strain rate deformation before the breakage. The strain rate jumps after the failure of the specimen at ~0.6 ms, where the corresponding strain is ~ 0.02. Figure 5.1(c) shows a typical set of stress equilibrium histories indicating that the incident end stress almost overlaps with the transmission end stress, especially before the specimen failure. Figure 5.1(d) shows all the stress strain curves obtained at ~100/s, where the specimen is printed in cylindrical shape from the first on-demand printing service vendor [45].

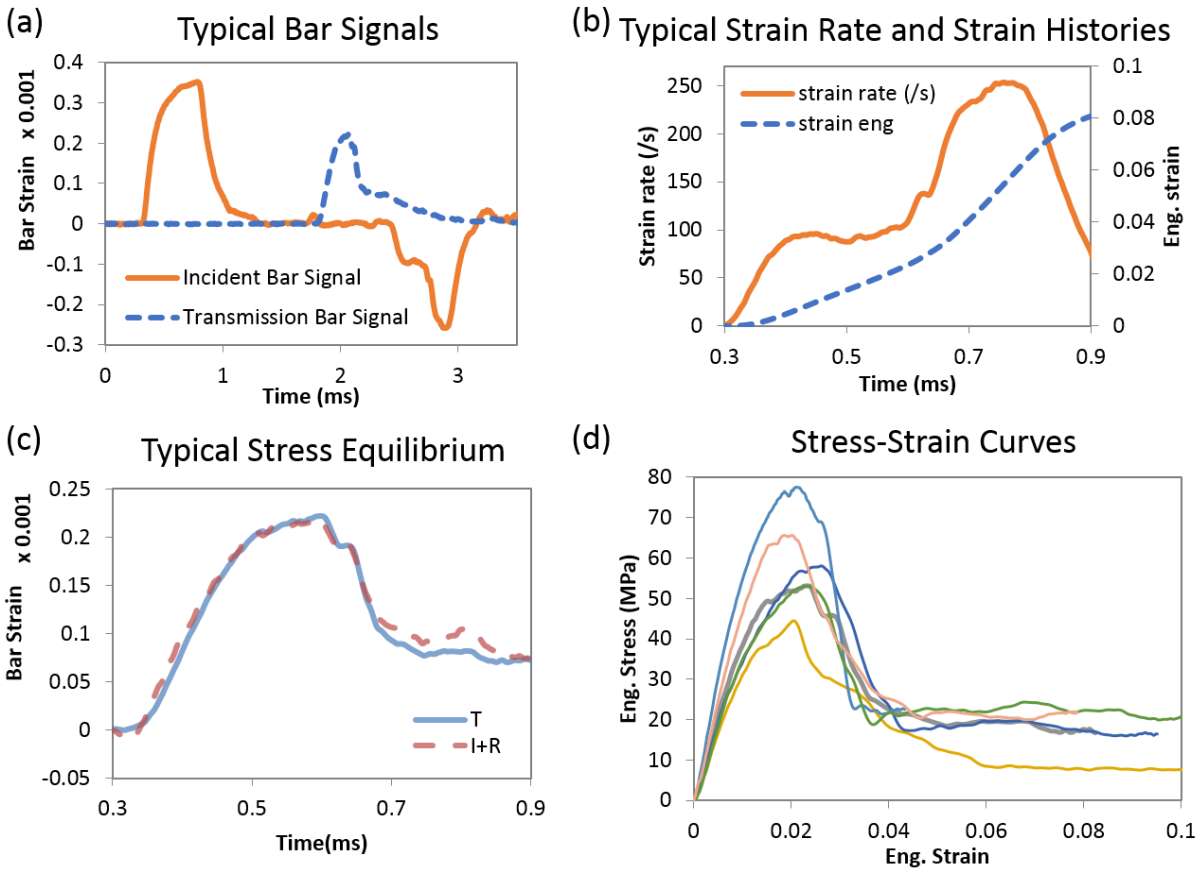

Figure 5.1 Experimental conditions and stress strain curves for the 3D printed sandstone specimens in cylindrical shape from the first vendor: (a) typical bar signals, (b) typical strain rate and strain histories, (c) typical stress equilibrium histories, and (d) stress strain curves at ~100/s strain rate for specimen from the first vendor.

The average stress strain curves for specimens obtained from the second vendor is shown in Figure 5.2. The strain rate for these stress strain curves is similar to the condition in Figure 5.1 for the specimens from the first vendor. From these results one can find that for both cylindrical specimens the initial module is similar, and after initial failure both specimens reach relatively plateau stress regions instead of sudden stress dropping to zero. However, the stress level and scatter from the first vendor cylindrical specimens are apparently larger than those from the second vendor. On the other hand, the stress strain curves apparently dependent on the shape of the specimen: the ring shape specimen gives the highest compressive strength, the cylindrical one gives the lowest compressive strength. It is noted that the cross-sectional area and length for both specimens are nearly the same.

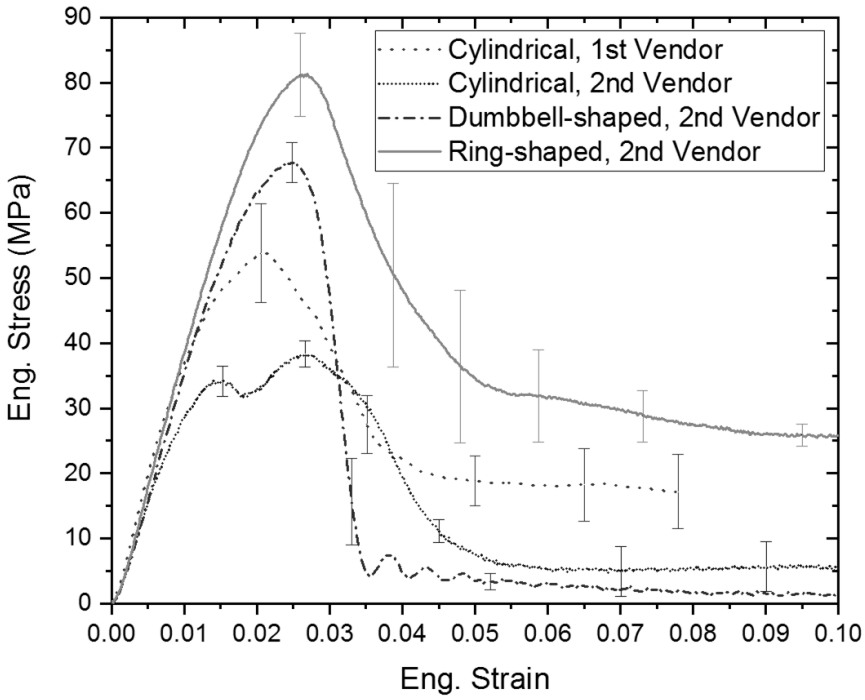

Figure 5.2 Average stress strain curves for 3D printed sandstone specimens in various types of shape.

As mentioned earlier, the ColorBond infiltrant coating has apparent effects on the strength of the printed sandstone. It is suspected that such coating has an apparent thickness that cannot be ignored. To verify this assumption, a specimen from each batch were cut open to examine the cross section. As shown in Figure 5.3, the inner rectangular area is the inner core of the specimen, where the material hardness is smaller than the outside rectangular ring. The outside rectangular ring is assumed to be the area where the ColorBond infiltrant coating penetrated. The thickness of the coated layer varies from 1.8 to 2.3 mm for the specimens printed from the first vendor, and from 1.35 to 1.6 mm for the specimens printed from the second vendor. It appears that the specimen with higher percentage of coated area leads to higher strength. The strengths for all four specimen types (three shapes from two vendors) are plotted in Figure 5.4. The percentage of coating from cross section (α) is calculated based on Equation 5.1, where the r is the radius of the specimen (gauge section) and t is the measured thickness from the specimen been cut open. The red dot is from cylindrical specimen via the first vendor and the blue dots are from the second vendor. From Figure 5.4, it is confirmed the assumption that higher percentage of coated area leads to higher strength, and the data from both vendor seems fall in one line.

$$\alpha = \frac{r^2 - (r-t)^2}{r^2} \tag{5.1}$$

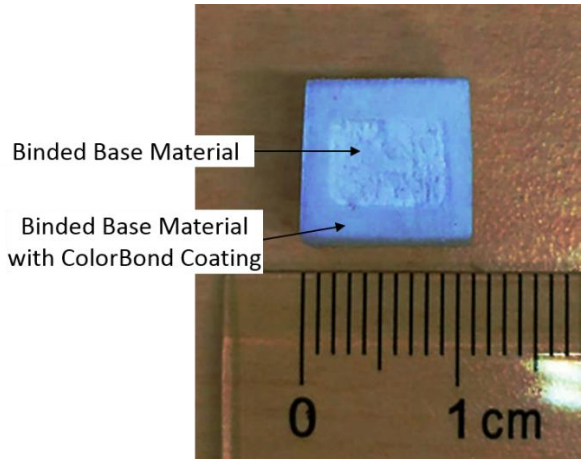

Figure 5.3 Cross-section of a 3D printed sandstone specimen.

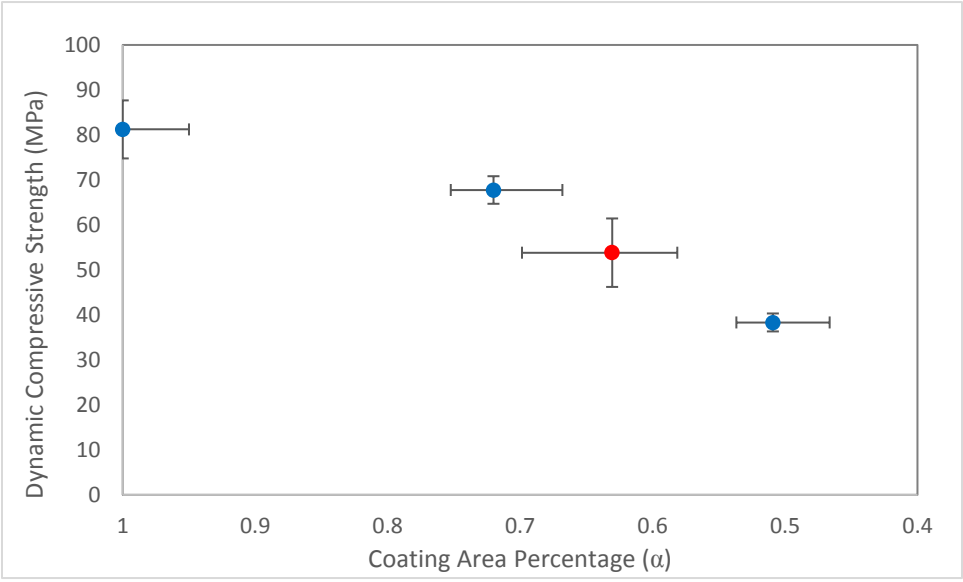

Figure 5.4 Dynamic compressive strength of 3D printed sandstone as a function of the ColorBond infiltrant coating percentage in specimen cross section.

5.3 2D Projections and Tomography Reconstructions

Figure 5.5 shows four projections taken for the same specimen (cylindrical from the first vendor) at four different points of delay time. The corresponding location in the stress strain curve of this specimen is shown in the left part of Figure 5.5. It can be found that before the peak stress (projection (a) and (b)), no apparent crack is visible. Right after the initial breakage (projection (c)), a crack can be visualized near the edge of the specimen, where the crack has the access to one of the bar end. At about 7.9% strain (projection (d)), two cracks are visible near the surface of the specimen. Both cracks are longer than the crack in projection (c), and both have access to the bar end. It is assumed that the crack is initiated from or near the bar end.

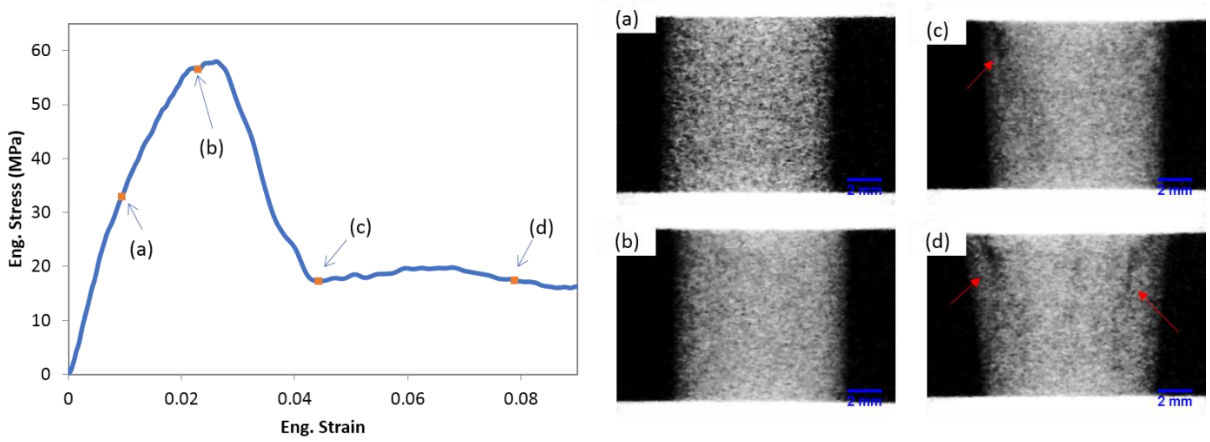

Figure 5.5 2D projections of a cylindrical 3D printed sandstone specimen with corresponding stress strain curve, where the four projections were taken for the same specimen at four different delay time.

Figure 5.6 shows the tomography reconstruction of a cylindrical specimen. The X-ray was fired at the specimen strain = 0.086. Figure 5.6(b) shows the 2D projections taken for this specimen, where in channels 1, 2 and 4 one can visualize two possible cracks and in channel 2 one possible crack can be seen (the other crack might be perpendicular to channel 2 thus cannot be visualized in 2D). It is noted that, the log attenuation at the center of the specimen is only ~0.6, which might result in a higher noise level compared to the case of machinable ceramics in section 4. Figure 5.6(c) shows the colorized volume view of reconstructed un-deformed specimen. From which one can find the specimen in cylindrical shape without cracks. Figure 5.6(d) shows the colorized volume views of reconstructed deformed specimen. Volume views from two different angles are presented,

where two cracks can be found. It is noted that the crack indicated by yellow colored arrow in left figure and right figure of 5.6(d) is the same crack but viewed in different angles. The direction for the yellow arrow indicated crack is ~20° to the loading axis and the direction for the red arrow indicated crack is ~50° to the loading axis. Both cracks have access to the bar end, which is similar to the case shown in Figure 5.5.

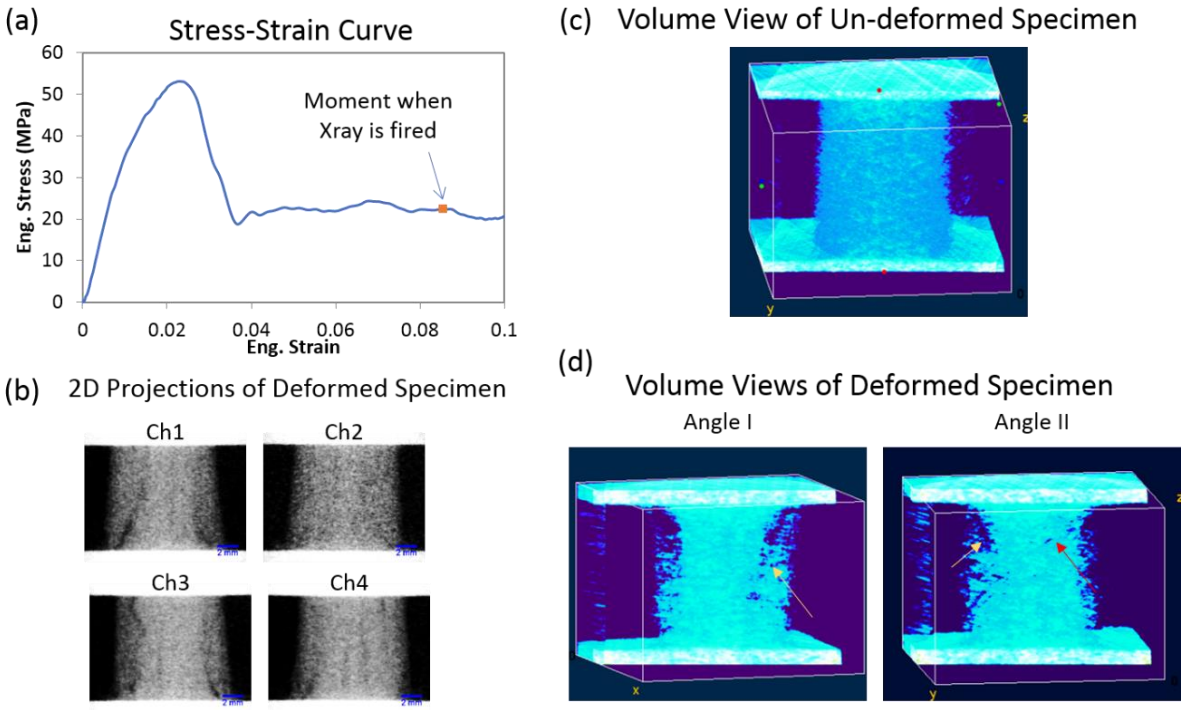

Figure 5.6 In-situ tomography reconstruction of a cylindrical 3D printed sandstone specimen: (a) stress strain curve and corresponding X-ray firing point, (b) 2D projections of deformed specimen, (c) colorized volume view of reconstructed un-deformed specimen, and (d) colorized volume views of reconstructed deformed specimen.

5.4 Discussions

The crack shown in Figure 5.6(d) matches with the recovered debris of the specimen, which is shown in Figure 5.7(b). Three pieces of debris were recovered: two in cone shape and one in thin-shell shape. It appears that the cracks in Figure 5.6(d) lead to the separation of the ColorBond coated layer on the side wall of the cylindrical specimen. Under dynamic loading conditions, it is possible that the ColorBond adhesive infiltrant becomes brittle under tension. Although there is no

mechanical data exist for this particular type of adhesive, researchers have reported several structural epoxies to behave ductile under quasi-static and dynamic compression but brittle under dynamic tensile conditions [47, 48]. Figure 5.7(a) shows a cross-sectional diagram of a cylindrical specimen under uniaxial compression, where the solid blue region indicates the coated region which has higher strength than the non-coated region (indicated by blue dots). Due to Poisson's Ratio, the side wall of the specimen would expend in lateral direction (being pushed out by the non-coated region). It can be found from Figure 5.3 that the curvature of the connection between side wall and top wall & bottom wall is small, which might result in stress concentration in the connection spots, as indicated by black lines in Figure 5.7(a). It is suspected the crack initialed due to such stress concentration and the brittleness of the coated layer under dynamic local tensile stress.

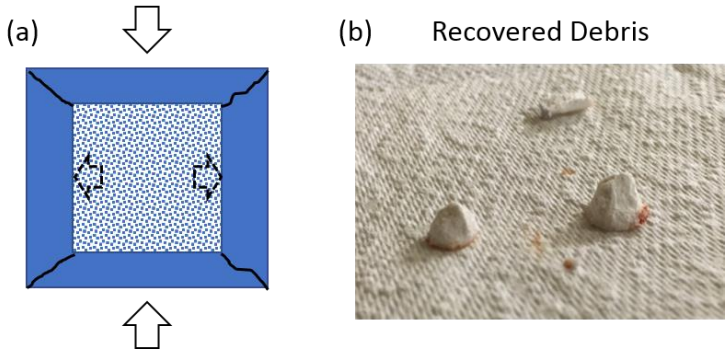

Figure 5.7 Dynamic fracture of cylindrical 3D printed sandstone specimen: (a) assumption of dynamic fracture mechanism based on weak spots, (b) recovered debris of the fractured specimen.

Since the coated layer might behave differently under quasi-static loading conditions. The same type of cylindrical specimen was compressed by a MTS 810 machine at 0.001/s strain rate. As shown in Figure 5.8(a), at 0.001/s, the material behaves in a ductile manner while the dynamic stress strain behavior is brittle. The dynamic peak stress (~55 MPa) is apparently higher than the stress in quasi-static (~22 MPa). Interestingly, the post failure plateau stress level from dynamic loading is similar to the yield stress level at quasi-static rate.

Figure 5.8(b) shows approximate strain mapping of the deformed specimen. Speckle patterns were spray painted on specimen surface. The deformation process is captured in sequence of photos via a Canon T2i DSLR with a Canon EF 100mm f/2.8 Macro lens. The time between frames is 10-sec,

indicating an interval of 0.01 nominal strain. The images were processed via an open source digital image correlation software ncorr [49]. It is noted that due to the specimen is in cylindrical shape, the Exx (lateral strain) shown in Figure 5.8(b) is an approximate to the real strain values, since the specimen surface is mapped onto the imaging plane. For qualitative analysis, the first crack initialed between strain values of 0.17-0.18. The location of the crack initiation point is at the center of the specimen, which is different from the dynamic case. Shear stress is the main driving stress for the crack to initial, as the crack is ~ 24° to the loading direction. The strain where the first crack is found under quasi-static loading is apparently larger than under dynamic loading.

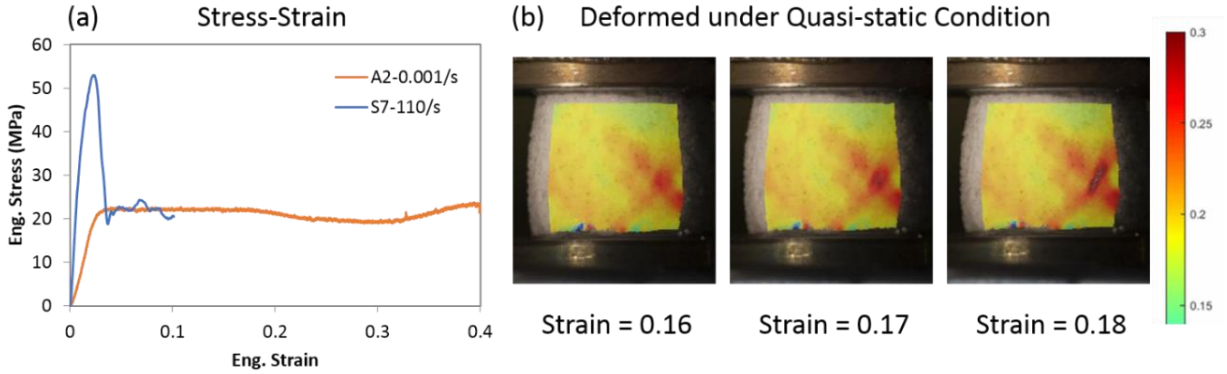

Figure 5.8 Quasi-static deformation of a cylindrical 3D printed sandstone specimen: (a) stress strain curve from 0.001/s comparing to 110/s, (b) approximate lateral strain mapping of the deformed specimen at 0.16, 0.17 and 0.18 nominal strain using digital image correlation.

Figure 5.9 shows the in-situ tomography reconstruction for the ring-shaped specimen and the dumbbell-shaped specimen. It can be found that the ring-shaped specimen also breaks from the specimen-bar interface (similar to cylindrical specimen), and the dumbbell-shaped specimen breaks from the center (gauge section).

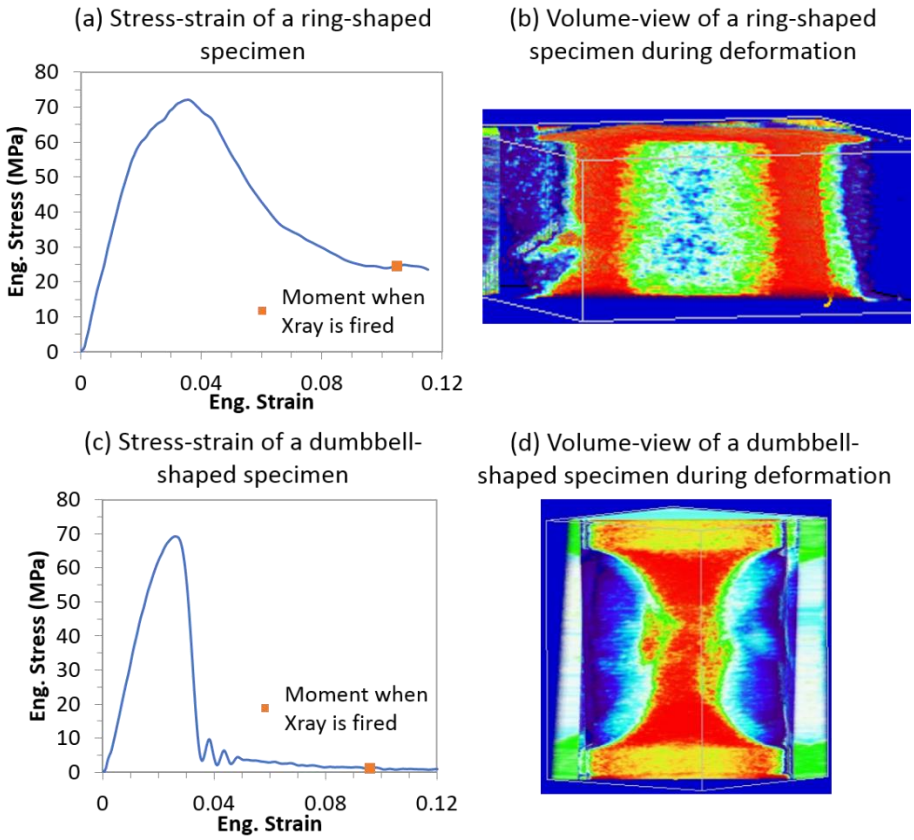

Figure 5.9 In-situ tomography reconstruction of ring-shaped and dumbbell-shaped 3D printed sandstone specimens.

5.5 Summary

In this section, dynamic uniaxial compression on 3D printed sandstone were conducted to examine the mechanical responses and failure mechanisms. The specimen exhibits brittle behavior under ~100/s strain rate loading. It is found that the adhesive infiltrant coated layer thickness apparently influences the mechanical behaviors. The specimen with higher percentage of coated layer has a higher dynamic compressive strength. Using in-situ flash X-ray tomography, the cylindrical and ring-shaped specimens are found to fracture leading by cracks initialed near specimen-bar interface under dynamic loading. The dumbbell-shaped specimen is found to fracture from its gauge section. For cylindrical specimen, it appears such cracks separate the infiltrant coated layer from the main body. On the other hand, the specimen under quasi-static loading exhibits ductile behavior, where the first crack initialed from the center of the specimen.

CHAPTER 6. LIMITATIONS AND FUTURE WORKS

From chapter 3-5, it can be found that the flash X-ray tomography is limited to reconstruct the volume with limited number of features (or cracks). For a dense dataset with sufficient feature-signal-to-noise ratio, it is capable to clearly define at least two cracks, if the crack directions roughly align with any of the X-ray beams (such as the plate-ball compression of aventurine spheres and indentation of machinable ceramics). In the case of the crack does not perfectly aligns with the X-ray beam but the feature still have enough signal-to-noise ratio, the reconstruction normalizing the deformed specimen projection with the corresponding un-deformed state can apparently improve the reconstruction quality. However, such normalizing would magnify the noise since the input is the difference between two images with random noise. Thus, for the features with low signal-to-noise ratio (such as the low attenuation chalk or the crack/void which size is small in all directions), it seems that the only way to achieve a reasonable reconstruction is to reduce the noise.

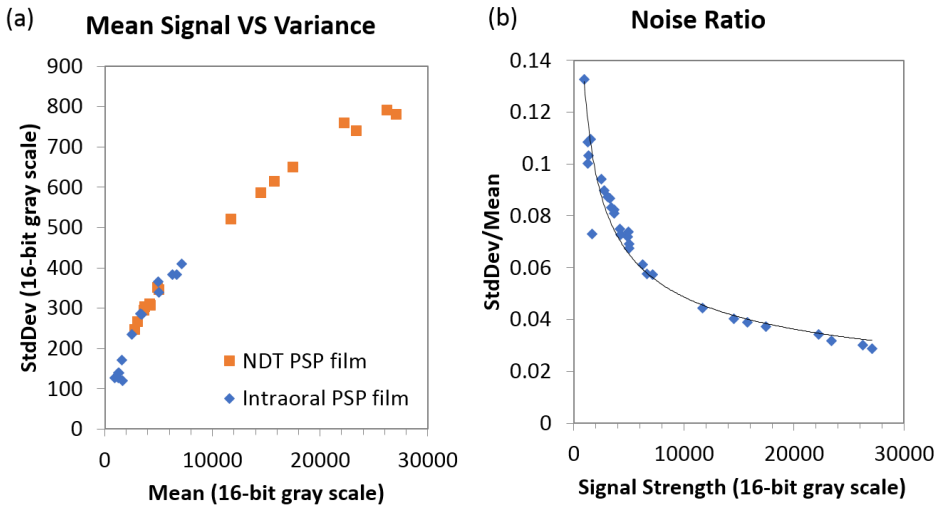

Figure 6.1 Projection noise as a function of signal strength for intraoral PSP and NDT PSPs: (a) standard deviation of a uniform background vs mean signal strength, and (b) noise ratio vs mean signal strength.

To reduce the noise, using higher intensity and a different type of PSP are proposed. It is found that a higher signal strength leads to lower noise ratio (as shown in Figure 6.1). In current research,

the noise ratio for the white background (incoming X-ray without attenuation) is about 6-8%. By adopting NDT PSP films, the corresponding white background noise ratio can reduce to 3-4%.

However, the NDT PSP has a larger size and large bending radius. The NDT PSP might have an apparent curvature when assembled to the existing imaging detector fixture (Figure 2.5(b)). A new fixture needs to be designed and the reconstruction algorithm needs to be modified to suit fan-beam application instead of parallel-beam. What's more, relocating the X-ray source closer would also improve the signal strength, which might also need a fan-beam based algorithm. Decreasing the source-specimen distance, on the other hand, might increase the geometric unsharpness (more blur).

Currently, the number of projections is limited to 4. As mentioned in chapter 2, higher number of projections leads to improved reconstruction quality. However, higher number of projections means a longer detector-specimen distance, for the detectors not in interference. To maintain a similar geometric unsharpness, one needs to put the X-ray source far away, which contradicts the requirement of high signal-to-noise ratio. The author suspects there exists an optimum combination of signal-to-noise ratio, geometric unsharpness and number of projections, which can be a part of future work.

It is noted the current reconstruction algorithm of ART does not involve any regularization. By considering the noise model (Figure 6.1) and applying the edges and boundary penalization of the reconstructed volume, future improvements can be made. The regularization can be applied by adding additional term in the algorithm to form a constrained optimization problem, where the algorithm minimizes the difference between the simulated projections from reconstructed volume and the experimental projections ($R_i - R_i^q$ in Equation 2.5) plus a prior term. An example of the prior term can to penalize the greyscale difference between neighboring voxels. Some advanced reconstruction algorithms can also be adopted, such as thresholded sparse object reconstruction [54] to further improve the reconstruction by normalizing the deformed projection with the un-deformed state, and soft discrete algebraic reconstruction technique [55] by assuming the reconstructed voxel can only be few discrete values for the dense dataset. For the application of typical Kolsky bar experiments, discrete reconstruction is promising since the dataset is dense.

CHAPTER 7. CONCLUSIONS

In this dissertation, Kolsky bar flash X-ray tomography methodology was developed to capture snapshots of the dynamic in-situ 3D specimen volume information. The 4-channel flash X-ray tomography experimental setup is built for (1) precise and repeatable control over the loading history of the specimen and the X-ray projection time, thus a correlation between the stress-strain/force-displacement response and the reconstructed volume can be clearly defined; and (2) low geometric unsharpness (0.15 mm) to improve reconstruction resolution by placing intraoral size PSP detectors close to the specimen without interference from unnecessary exposures.

Image processing techniques was developed to transform raw 2D projection images to 3D tomography reconstructions. Alignment of the images was performed by aligning the Kolsky bars in the image after edge detection. Dark current was measured for each experiment and imposed to the reconstruction log input. The log inputs with and without the normalization to the un-deformed state were used. In some dense dataset scenarios, the method with un-deformed state normalization outperforms the method without normalization. Algebraic Reconstruction Technique was used to iteratively update the reconstruction, since it reduces the number of artifacts comparing to Radon-transformation-based algorithms, especially when the number of projections is limited to 4.

Three static phantom reconstructions and three sets of preliminary experiments were conducted to verify the method and explore the application range. The result from phantoms shows the image processing inputs are correct and the relative locations of X-ray beams, specimen and PSP detectors are within the tolerance. The result from preliminary experiments implies that a good tomography reconstruction requires a reasonable specimen log attenuation for a sufficient feature-signal-to-noise ratio and a small number of cracks inside the specimen for reduced artifacts.

To apply the developed techniques, dynamic spheroconical indentation experiments on two types of machinable ceramics (Macor and M/M) and uniaxial compression on 3D printed sandstone around 100/s strain rate were conducted to examine the mechanical responses and failure mechanisms. The in-situ tomography reconstructions show that the Macor specimen breaks due to two major cracks - one parallel and the other oblique to the loading direction, while the M/M specimen fractures due to only one major crack parallel to the loading. Such finding matches with the cross-sectional microstructure images, which show that the Macor particle is randomized distributed, while the M/M particle is highly directional. The adhesive infiltrant coated layer in 3D

printed sandstone apparently influences its mechanical behaviors: the specimen with higher percentage of coated layer has higher strength. Under dynamic loading, the 3D printed sandstone exhibits brittle behavior, and the images show the cylindrical specimen fractures due to cracks initialed near specimen-bar interface. Under quasi-static loading, however, the sandstone exhibits ductile behavior, and the crack is initialed from the center of the specimen. Based on the reconstruction results, the flash X-ray tomography is currently limited to visualize specimens with few number of features, where such features need to have sufficient signal-to-noise ratio to the neighboring in at least one 2D projection. Several possible improvement methods (reducing the 2D projection noise, increasing number of projections, and using regularization-based reconstruction algorithms) are also discussed.

REFERENCES

[1] Kolsky, Herbert. "An investigation of the mechanical properties of materials at very high rates of loading." Proceedings of the Physical Society. Section B 62, no. 11 (1949): 676.

[2] Chen, Weinong W., and Bo Song. Split Hopkinson (Kolsky) bar: design, testing and applications. Springer Science & Business Media, 2010.

[3] GRAY III, George T. "Classic split Hopkinson pressure bar testing." ASM Handbook, Mechanical testing and evaluation 8 (2000): 462-476.

[4] Frew, D. J., M. J. Forrestal, and W. Chen. "Pulse shaping techniques for testing elastic-plastic materials with a split Hopkinson pressure bar." Experimental mechanics 45, no. 2 (2005): 186.

[5] Harding, J., E. O. Wood, and J. D. Campbell. "Tensile testing of materials at impact rates of strain." Journal of Mechanical Engineering Science 2, no. 2 (1960): 88-96.

[6] Duffy, J., J. D. Campbell, and R. H. Hawley. "On the use of a torsional split Hopkinson bar to study rate effects in 1100-0 aluminum." Journal of Applied Mechanics 38, no. 1 (1971): 83-91.

[7] Frew, Danny J., Stephen A. Akers, W. Chen, and Mark L. Green. "Development of a dynamic triaxial Kolsky bar." Measurement Science and Technology 21, no. 10 (2010): 105704.

[8] Gilat, A., T. E. Schmidt, and A. L. Walker. "Full field strain measurement in compression and tensile split Hopkinson bar experiments." Experimental Mechanics 49, no. 2 (2009): 291-302.

[9] Chen, Weinong W., Matthew C. Hudspeth, Ben Claus, Niranjan D. Parab, John T. Black, Kamel Fezzaa, and S. N. Luo. "In situ damage assessment using synchrotron X-rays in materials loaded by a Hopkinson bar." Phil. Trans. R. Soc. A372, no. 2015 (2014): 20130191.

[10] Sutton, Michael A., Jean Jose Orteu, and Hubert Schreier. Image correlation for shape, motion and deformation measurements: basic concepts, theory and applications. Springer Science & Business Media, 2009.

[11] Zoltani, C. K., K. J. White, and F. A. DiBianca. "Multichannel flash x-ray tomography of microsecond events." Applied optics24, no. 23 (1985): 4061-4063.

[12] Moser, Stefan, Siegfried Nau, Manfred Salk, and Klaus Thoma. "In situ flash x-ray high-speed computed tomography for the quantitative analysis of highly dynamic processes." Measurement Science and Technology 25, no. 2 (2014): 025009.

[13] http://www2.l-3com.com/ati/solutions/irs.htm

[14] Canny, John. "A computational approach to edge detection." In Readings in Computer Vision, pp. 184-203. 1987.

[15] MessaoudiI, Cédric, Thomas Boudier, Carlos Oscar Sanchez Sorzano, and Sergio Marco. "TomoJ: tomography software for three-dimensional reconstruction in transmission electron microscopy." BMC bioinformatics 8, no. 1 (2007): 288.

[16] Mohan, K. Aditya, S. V. Venkatakrishnan, John W. Gibbs, Emine Begum Gulsoy, Xianghui Xiao, Marc De Graef, Peter W. Voorhees, and Charles A. Bouman. "TIMBIR: A method for time-space reconstruction from interlaced views." IEEE Transactions on Computational Imaging 1, no. 2 (2015): 96-111.

[17] Liao, H. Y., and G. T. Herman. "Direct Image Reconstruction-Segmentation, as Motivated by Electron Microscopy." In Advances in Discrete Tomography and Its Applications, pp. 247-270. Birkhäuser Boston, 2007.

[18] Moy, Paul, Tusit Weerasooriya, Wayne Chen, and Alex Hsieh. "Dynamic stress-strain response and failure behavior of PMMA." In ASME 2003 International Mechanical Engineering Congress and Exposition, pp. 105-109. American Society of Mechanical Engineers, 2003.

[19] Song, B., C. J. Syn, C. L. Grupido, W. Chen, and W-Y. Lu. "A long split Hopkinson pressure bar (LSHPB) for intermediate-rate characterization of soft materials." Experimental mechanics 48, no. 6 (2008): 809.

[20] Grandt Jr, Alten F. Fundamentals of structural integrity: damage tolerant design and nondestructive evaluation. John Wiley & Sons, 2003.

[21] http://www.ndt-ed.org/

[22] Germer, Rudolf. "X-ray flash techniques." Journal of Physics E: Scientific Instruments 12, no. 5 (1979): 336.

[23] Chen, Weinong W., and Dimitri Peroulis. Impact Response of Granular Material at Global and Meso Scales. No. DTRA-TR-12-66. PURDUE UNIV LAFAYETTE IN, 2013.

[24] Fugelso, Erik. Material density measurements from dynamic flash x-ray radiographs using axisymmetric tomography. No. LA-8785-MS. Los Alamos Scientific Lab., NM (USA), 1981.

[25] Lin, Yong, Jingjin Wang, and Zheng Song. "Gelatin cavity 3-D reconstruction from flash X-ray images of wound ballistics." JOURNAL-TSINGHUA UNIVERSITY 42, no. 12 (2002): 1576-1578.

[26] http://www.airtechniques.com/

[27] U.S. National Archives and Records Administration. 1991. Code of federal regulations. Title 10. Standards for Protection Against Radiation.

[28] Hubbell, John H., and Stephen M. Seltzer. Tables of X-ray mass attenuation coefficients and mass energy-absorption coefficients 1 keV to 20 MeV for elements Z= 1 to 92 and 48 additional substances of dosimetric interest. No. PB--95-220539/XAB; NISTIR--5632. National Inst. of Standards and Technology-PL, Gaithersburg, MD (United States). Ionizing Radiation Div., 1995.

[29] Gordon, Richard, Robert Bender, and Gabor T. Herman. "Algebraic reconstruction techniques (ART) for three-dimensional electron microscopy and X-ray photography." Journal of theoretical Biology 29, no. 3 (1970): 471-481.

[30] Kim, Joshua, Huaiqun Guan, David Gersten, and Tiezhi Zhang. "Evaluation of algebraic iterative image reconstruction methods for tetrahedron beam computed tomography systems." Journal of Biomedical Imaging 2013 (2013): 8.

[31] Oliveira, Eric F., Sílvio B. Melo, Carlos C. Dantas, Daniel AA Vasconcelos, and F. Cadiz. "Comparison among tomographic reconstruction algorithms with a limited data." In International Nuclear Atlantic Conference-INAC 2011. 2011.

[32] Mishra, Debasish, Jon P. Longtin, Raman P. Singh, and Vishwanath Prasad. "Performance evaluation of iterative tomography algorithms for incomplete projection data." Applied optics 43, no. 7 (2004): 1522-1532.

[33] Frew, D. J., MICHAEL J. Forrestal, and W. Chen. "A split Hopkinson pressure bar technique to determine compressive stress-strain data for rock materials." Experimental mechanics41, no. 1 (2001): 40-46.

[34] Richard, Julie, Mai-Linh Doan, Jean-Pierre Gratier, and François Renard. "Microstructures induced in porous limestone by dynamic loading, and fracture healing: an experimental approach." Pure and Applied Geophysics 172, no. 5 (2015): 1269-1290.

[35] Petrov, Yuri V., Ivan V. Smirnov, Grigory A. Volkov, Andrei K. Abramian, Anatoliy M. Bragov, and Stanislav N. Verichev. "Dynamic failure of dry and fully saturated limestone samples based on incubation time concept." Journal of Rock Mechanics and Geotechnical Engineering 9, no. 1 (2017): 125-134.

[36] http://www.crystexllc.com/

[37] https://www.corning.com/

[38] Sneddon, Ian N. "The relation between load and penetration in the axisymmetric Boussinesq problem for a punch of arbitrary profile." International journal of engineering science 3, no. 1 (1965): 47-57.

[39] Parab, Niranjan D., Zherui Guo, Matthew C. Hudspeth, Benjamin J. Claus, Kamel Fezzaa, Tao Sun, and Weinong W. Chen. "Fracture mechanisms of glass particles under dynamic compression." International Journal of Impact Engineering 106 (2017): 146-154.

[40] Tymrak, B. M., M. Kreiger, and Joshua M. Pearce. "Mechanical properties of components fabricated with open-source 3-D printers under realistic environmental conditions." Materials & Design 58 (2014): 242-246.

[41] Khaing, M. W., J. Y. H. Fuh, and L. Lu. "Direct metal laser sintering for rapid tooling: processing and characterisation of EOS parts." Journal of Materials Processing Technology 113, no. 1-3 (2001): 269-272.

[42] Seitz, Hermann, Wolfgang Rieder, Stephan Irsen, Barbara Leukers, and Carsten Tille. "Three-dimensional printing of porous ceramic scaffolds for bone tissue engineering." Journal of Biomedical Materials Research Part B: Applied Biomaterials74, no. 2 (2005): 782-788.

[43] Ledingham, Austin D., Jeryl D. English, Sercan Akyalcin, Benjamin E. Cozad, Joe C. Ontiveros, and F. Kurtis Kasper. "Accuracy and mechanical properties of orthodontic models printed 3-dimensionally from calcium sulfate before and after various postprinting treatments." American Journal of Orthodontics and Dentofacial Orthopedics 150, no. 6 (2016): 1056-1062.

[44] Osinga, S., G. Zambrano-Narvaez, and R. J. Chalaturnyk. "Study of geomechanical properties of 3D printed sandstone analogue." In 49th US Rock Mechanics/Geomechanics Symposium. American Rock Mechanics Association, 2015.

[45] https://www.3dhubs.com/

[46] https://www.3dsystems.com/

[47] Goglio, Luca, Lorenzo Peroni, Marco Peroni, and Massimo Rossetto. "High strain-rate compression and tension behaviour of an epoxy bi-component adhesive." International journal of adhesion and adhesives 28, no. 7 (2008): 329-339.

[48] Al-Zubaidy, Haider, Xiao-Ling Zhao, and Riadh Al-Mahaidi. "Mechanical characterisation of the dynamic tensile properties of CFRP sheet and adhesive at medium strain rates." Composite Structures 96 (2013): 153-164.

[49] Blaber, J., B. Adair, and A. Antoniou. "Ncorr: open-source 2D digital image correlation matlab software." Experimental Mechanics 55, no. 6 (2015): 1105-1122.

[50] Siviour, C. R., and W. G. Proud. "Damage formation during high strain rate deformation of PBS9501." In AIP Conference Proceedings, vol. 955, no. 1, pp. 799-802. AIP, 2007.

[51] Parab, Niranjan D., Benjamin Claus, Matthew C. Hudspeth, John T. Black, Alex Mondal, Jianzhuo Sun, Kemal Fezzaa, Xianghui Xiao, S. N. Luo, and Wayne Chen. "Experimental assessment of fracture of individual sand particles at different loading rates." International Journal of Impact Engineering 68 (2014): 8-14.

[52] Anton, Richard J., and Ghatu Subhash. "Dynamic Vickers indentation of brittle materials." Wear 239, no. 1 (2000): 27-35.

[53] Yang, Fuqian. "Thickness effect on the indentation of an elastic layer." Materials Science and Engineering: A 358, no. 1-2 (2003): 226-232.

[54] Li, Meihua, Hiroyuki Kudo, Jicun Hu, and Roger H. Johnson. "Improved iterative algorithm for sparse object reconstruction and its performance evaluation with micro-CT data." IEEE Transactions on Nuclear Science 51, no. 3 (2004): 659-666.

[55] Bleichrodt, Folkert, Frank Tabak, and Kees Joost Batenburg. "SDART: An algorithm for discrete tomography from noisy projections." Computer Vision and Image Understanding 129 (2014): 63-74.

PUBLICATIONS

1. Liao, Hangjie and Weinong W. Chen. "Specimen/bar Impedance Mismatch on Equilibrium and Rate Constancy in Kolsky Bar." Experimental Mechanics (submitted)

2. Nie, Yizhou, Hangjie Liao, and Weinong W. Chen. "Cyclic tensile response of a pre-tensioned polyurethane." Mechanics of Time-Dependent Materials (2017): 1-13.

3. Claus, B., J. Chu, M. Beason, H. Liao, B. Martin, and W. Chen. "Dynamic Experiments using Simultaneous Compression and Shear Loading." Experimental Mechanics57, no. 9 (2017): 1359-1369.

4. Tsutsui, W., T. Siegmund, N. D. Parab, H. Liao, T. N. Nguyen, and W. Chen. "State-of-Charge and Deformation-Rate Dependent Mechanical Behavior of Electrochemical Cells." Experimental Mechanics (2017): 1-6.

5. Lim, Boon Him, Hangjie Liao, Weinong W. Chen, and Michael J. Forrestal. "Effects of constant engineering and true strain rates on the mechanical behavior of 304 stainless steel." Journal of Dynamic Behavior of Materials 3, no. 1 (2017): 76-82.

6. Kukreja, J., T. Nguyen, T. Siegmund, W. Chen, W. Tsutsui, K. Balakrishnan, H. Liao, and N. Parab. "Crash analysis of a conceptual electric vehicle with a damage tolerant battery pack." Extreme Mechanics Letters 9 (2016): 371-378.

7. Nguyen, Trung N., Thomas Siegmund, Waterloo Tsutsui, Hangjie Liao, and Wayne Chen. "Bi-objective optimal design of a damage-tolerant multifunctional battery system." Materials & Design 105 (2016): 51-65.

8. Tsutsui, Waterloo, Trung Nguyen, Hangjie Liao, Niranjan Parab, Jaspreet Kukreja, Thomas Siegmund, and Wayne Chen. "Mechanical energy dissipation in a multifunctional battery system." MRS Advances 1, no. 6 (2016): 381-388.

9. Lu, L., D. Fan, B. X. Bie, X. X. Ran, M. L. Qi, N. Parab, J. Z. Sun et al. "Note: dynamic strain field mapping with synchrotron X-ray digital image correlation." Review of Scientific Instruments 85, no. 7 (2014): 076101.

10. Czech, Christopher, Aaron J. Ward, Hangjie Liao, and Weinong W. Chen. "Investigating uncertainty in SHPB modeling and characterization of soft materials." In Challenges in Mechanics of Time-Dependent Materials, Volume 2, pp. 21-30. Springer, Cham, 2015.

11. Liao, H., W. Chen, and Vincent P. Chiarito. "Mechanical response of a soft rubber compound compressed at various strain rates." Mechanics of Time-Dependent Materials 18, no. 1 (2014): 123-137.